POLITECNICO DI TORINO

Master of Science in Energy and Nuclear Engineering

Master Thesis

ON THE EFFECT OF WICKING ON THE DROPLET COOLING

Supervisors:
Prof. Pietro Asinari
Prof. Carlos Dorao

Student:
Damiano Auliano

September 2018

Abstract

Several thermal management applications operating at low temperatures require the liquid to spread as much as fast as possible in order to improve the cooling performance. Due to the recent progresses in micro/nano technology, it is possible to control the wickability of a surface by texturing it with micro/nano-structures. However, still there is not a common method to characterize the wickabilty for super-hydrophilic surfaces . In order to assess the effect of wickability on the droplet cooling, a proper wicking method has been implemented and validated, and surfaces coated with nanowires with different wickability have been fabricated and characterized. In this work, it has been shown that controlling the wickability of the surface allows to tune the heat transfer performance. The tallest nanowire surface(h = 25.27 ± 0.08 μm) resulted in the highest wicking coefficient(w = 0.888 ± 0.076 mm/s$^{0.5}$) and in the best cooling performance. With respect to the plain Si, nanowires with the highest wicking performance showed a decrease in the evaporation time of 82 %, 76 % and 68 % at respectively 51 °C, 69 °C and 92 °C. Moreover, increasing the surface temperature, reduces the effect of the surface wickability on the cooling time.

Acknowledgements

Damiano Auliano

Contents

List of Figures

11

List of Tables

Chapter 1

Introduction

1.1 Motivation

Many thermal management and industrial applications, such as electronic cooling (CPU chips, telecom equipment, laser diodes), desalination, chemical processing (micro-chemical reactors), micro-fuel cell combustors, air conditioning and refrigeration require to remove ultra-high heat flux [3, 4, 5]. It is well known from thermodynamics that the phase-change has a high latent heat, therefore the boiling of a fluid represents the best way to remove it. Further, thermodynamics parameters such as wettability and wickability of the surface can help to improve the heat transfer [3, 4, 5] .

The need of controlling the wettability and wickability of the surface for improving the heat transfer from a surface to the cooling media has motivated the development of micro-nano engineered surfaces. In this regard, reducing the size of the micro-structures has the potential of improve the action of the capillary forces for enhancing the spreading the liquid on the surface. In this sense, designing organized sub-micron structures may allow to enhance the heat transfer from a surface to the cooling media substantially.

In particular, super-hydrophilic structures were tested to improve the nucleate boiling heat transfer and critical heat flux for pool boiling[6],to delay the incipience of the dryout in flow boiling[7], to enhance the droplet spreading and its evaporation in the phase exchange[8, 9] and increase the

temperature of the Leidenfrost point[10, 11].

However, the droplet evaporation has been mainly studied over surfaces with poor wettability[12]. Since there have been very few studies regarding this phenomenon over superhydrophilic surfaces[8], the main goal of this work is to investigate it over silicon random nanowires (NWs). In this regard, it is interesting to verify if the droplet spreading can affect the cooling performance during the evaporation. Therefore, a method for characterizing the wettability and wickability of these surfaces has been developed before proceeding with the heat transfer study.

1.2   Goal and objective

The primary goal of this work is to investigate the effect of the wickability on the droplet evaporation over Si random nanowires. In order to perform this, the following main tasks need to be accomplished:

- A literature review on the assessment of the wicking effect on the cooling heat transfer, with particular attention to the droplet evaporation. A state of art concerning the wicking methods has to be performed, with particular regard to the nanowires structures.

- Design a wicking facility and develop a Matlab code able to detect the spreading evolution of a droplet over a nanoporous material and also to detect the contact angle during the same transient.

- Validate the facility and the code developed.

- Perfom experiments of wettability and wickability on Si random nanowires and assess the measurements with a detailed uncertainty analysis.

- Perform the heat transfer experiments related to the droplet evaporation, and include also the nucleate boiling regime.

- Evaluate the effect of the wickability on the heat transfer performance.

1.3 Scope

This work focuses on determining the the evaporation and nucleate boiling curve of three different Si random NWs having three different wickabilities. From this result, the effect of the wickability can be observed and assessed. Prior to the heat transfer experiments, it is necessary to characterize systematically the wickability and wettability of the textured surfaces. Therefore, a proper method has to be developed in order to characterize the nanostructures.

1.4 Overview of the thesis

The main goal of this thesis is to investigate the effect of the wettability and wickability on the droplet evaporation over surfaces covered by random silicon nanowires.

- In the chapter 2, a theoretical background of droplet heat exchange, wettability and wickability is provided. Section 2.4 provides a state of art of wickability in relation to the droplet cooling heat transfer. Furthermore, a state of art on the different wicking methods is performed in order to highlight their limitations and figure out the best method for measuring it.

- In the section 3.1, a description of the wettability and wickability setup and an overview of the experimental procedure are provided.

- In the section 3.2, the development and the validation of the wicking and contact angle Matlab codes are described with relative uncertainty analysis.

- In the chapter 4, an overview of the fabrication and characterization of the samples are provided. Further, a systematic quantification of the wicking is provided. Finally, a benchmark analysis based on predictive models is performed.

- In the section 5.1, a description of the droplet evaporation setup is presented.

- In the sections 5.2 and5.3, a calibration of the themocouples and a validation of the facility are respectively performed.

17

- In the sections 5.4 and 5.5, experimental uncertanties and results are shown with further discussion.

- In the section 6, conclusions are summarized and further works are suggested.

Chapter 2

Theorethical background

2.1   General physics on the droplet evaporation

First experiments of evaporation droplet over heated surfaces were conducted by Wachters and Westerling in 1966[13] . It has been observed that many parameters can affect the heat exchange[14]. Among these, some are related to the droplet characteristics, as the diameter and the terminal velocity of impact, others are the thermodynamics liquid properties, that include the saturation temperature T_{sat}, density ρ_l, dynamic viscosity μ_l and surface tension σ_l. In addition, pressure, temperature and velocity of the surrounding fluid affect the heat transfer. A crucial role is represented by the geometric characteristics of the surface, such as wettability, wickability, roughness and temperature [14].

In particular, the last one determines the regime of the heat transfer. In the case of the droplet cooling, the heat transfer performance is assessed by determining the sessile droplet evaporation curve[15] . An example is shown in Figure 2.1, where the droplet lifetime is plotted versus the surface temperature.

The first regime is referred to be single phase regime, known as *film evaporation regime* [14]. The surface temperature T_{wall} is lower than the saturation temperature T_{sat} and the heat transfer mechanism is dominated by the conduction between the surface and the liquid. Furthermore, contact angle and contact area significantly change during the first stage from the
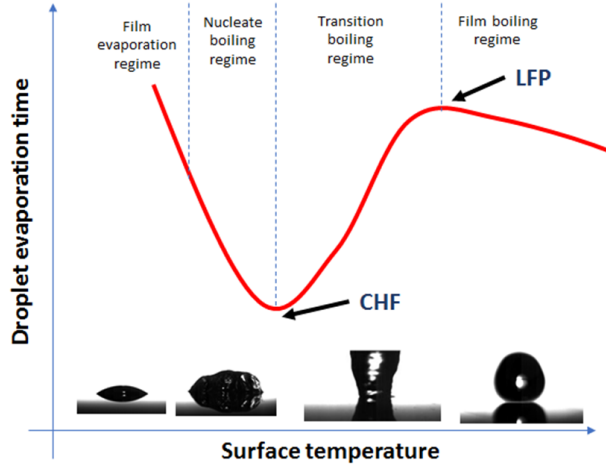
Figure 2.1: Sessile droplet evaporation curve

impact, by affecting significantly the heat transfer.

When the T_{wall} overcomes sufficiently the T_{sat}, a second regime occurs, which is properly known as *nucleate boiling regime* [14]. Bubbles are released from activated sites on the superheated surface. This two-phase regime is characterized by a high heat transfer coefficient due to the latent heat. This culminates with a minimum evaporation time, known as *critical heat flux* (CHF), which represents the best point in terms of the cooling performance.

The third regime is a transition regime in which a discontinuous layer of vapor exists between of the droplet and the solid surface. The heat transfer performance is deteriorated due to presence of the vapor that has a lower thermal conductivity. This regime is called *transition boiling regime* [14].

By increasing the surface temperature, the vapour layer becomes continuous. The minimum temperature at which this phenomenon occurs is called Leidenfrost point (LFP), that corresponds to the maximum droplet lifetime. The thin film vapour acts as a cushion layer for the droplet. From this point, the heat transfer coefficient is dramatically reduced due to the low thermal conductivity of the vapour. In this case, the mechanisms involving the heat transfer are the conduction and the irradiation (due to the high temperatures). This regime is called *film boiling regime*[14] and it is undesired since it damages the surface[16].

2.2   Basic concepts of wettability

Most of the energy applications are based on the phase change of a liquid in a pipe or a container. The way the two phases keep in touch with the wall can affect the heat and mass transfer [17]. Wettability can be defined as the affinity of a fluid has with a solid surface. This can be quantified by the contact angle.

The measurement of a contact angle is done by impinging a droplet over a solid surface. Under equilibrium condition, we can consider a plane perpendicular to the three-phase contact line. If we draw a line in that plane that is tangent to the gas-liquid interphase (droplet) and passes through the intersect point of the three phases, a contact angle θ is observed, as shown in Figure 2.2.
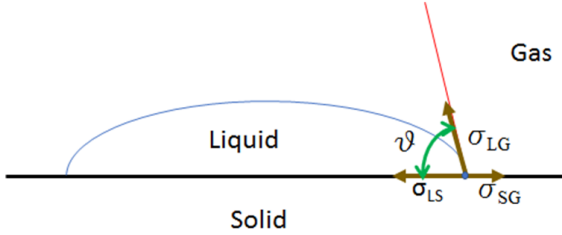
Figure 2.2: Contact angle anf the three phases under equilibrium condition

By considering the static equilibrium, the resulting equation is:

$$\sigma_{SG} = \sigma_{LS} + \sigma_{LG}\cos\theta \qquad (2.1)$$

where σ_{SG} is the interfacial tension between solid and gas, σ_{LG} is the interfacial tension between liquid and gas and σ_{LS} is the interfacial tension

between liquid and solid.

For 0°< θ < 90°, the liquid can be classified as a *wetting liquid*. For 90°< θ < 180°, it is instead named as *non wetting liquid*[17]. The surface is considered super-hydrophilic if θ is close very low and approximate to 0°, while it is said super-hydrophobic if θ > 150°.

However, the equilibrium equation described before is valid for idealized surface that are perfectly smooth. In the reality, there is a contact angle for any point of the contact line. In the ideal case the *actual(local) contact angle* would be equal to the ideal contact angle[18].

The contact angle measured experimentally should properly called *apparent(global) contact angle*, which can be defined as an average contact angle for all the three phase contact line.

2.3   Spreading and wicking phenomenon

The purpose of this work is to investigate on the effect of the droplet cooling upon a heated super-hydrophilic surface. It is therefore needed to undestand the physics of a droplet that is deposited on this type of surfaces.

According to the observations of our experiments and on the previous works, Figure 2.3 gives a physical explanation on what occurs during the spreading of a droplet on a super-hydrophilic and porous surface(in our case a nanopourous media). In the first stage that is called synchronous spreading[19], the upper part of the droplet collapses on the surface, while the bottom part gets inside the nanowire layer. The latter part of liquid spreads up to form a thin fringe, the so called precursor rim[20]. The droplet and precursor rim show a *synchronous* spreading.

The second stage is known to be as the hemispreading stage[19]. Here the precursor rim gets ahead of the contact line, and the upper droplet behaves like a source for the thin liquid in the array. In the meanwhile, the source continues to spread on the porous wetted surface.

The last stage shows the upper droplet to disappear into the porous layer, while the precursor rim continues to spread until the complete evaporation.
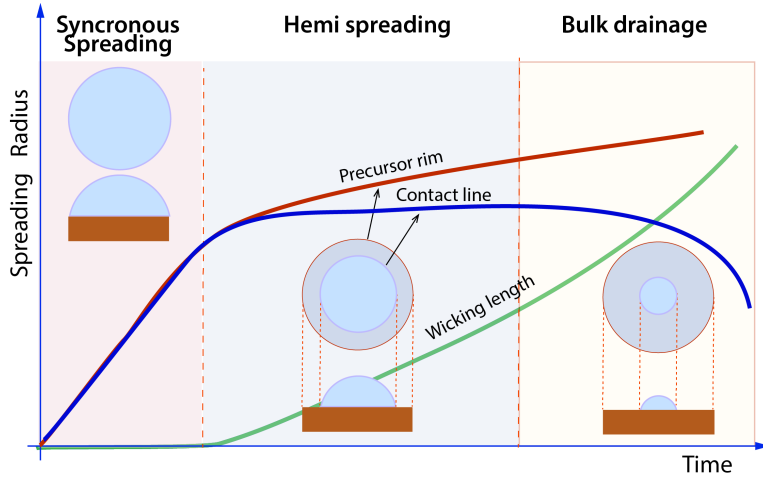
Figure 2.3: Physical behaviour of a droplet impinged on super-hydrophilic surface.

The porous media which will be investigated in this work are random nanopillars. They are supposed to show interesting benefits, such as an increase of the available area for the heat exchange, and also high wettability and capillary features. These properties can arise a particular interest in the field of the thermal management, especially in the case where thermal crisis occurs(boiling).

2.4 State of Art

Nowadays, reaching a proper design of a surface is getting always more important . In fact, the control of the wetting properties has increased enormously over the past few decades. These properties are strongly related to the spreading features of a surface, which for example can affect the efficiency of heat and mass transfer in evaporative coolers and condensers[20].

The spreading of a droplet on a surface, which can be properly indicated as wicking phenomenon, is strongly related to many industrial and biological applications, ranging from ranging from passive capillary-driven cooling technology, oil recovery, inject printing, DNA chips and drug delivery. Particular attention is related to the field of thermal management

23

in the electronic cooling[21, 22, 23], biomedical applications[24] and sensor devices[25].

If the wicking occurs over surfaces with an higher temperature of the droplet, a transient heat exchange occurs. An higher spreading of the thin film would mean a larger heat transfer area. Further, the lower thickness of the film implies a decrease in the conductive thermal resistance, which increaseas both the temperature of the droplet surface and the heat transfer transferred to the liquid-vapour phase[26]. A strong spreading would also reduce the possibility of phenomena like the splashing, bouncing and breaking of the droplet (include reference). This might imply a more efficient heat exchange (the area is not affected) and usage in terms of amount of liquid, such as in spray cooling or applications where the liquid source is limited [8].

Anyway, the assessment of the wicking effect on the droplet evaporation and on the nucleate boiling has not been clearly demonstrated and properly investigated. On the contrary, there have been some studies that relate the wicking to phenomena that occur in other regimes at very high temperatures.

Recent studies demonstrated the wicking to be the fundamental mechanism for avoiding the burnout surface of the surface in pool boiling and flow boiling experiments. Regarding the pool boiling, Rahman et al. (2014) and Shim et al.(2017) showed that wicking on super-hydrophilic surface can tune the CHF[27, 28]. In 2016, Kim et al. reported the same on the flow boiling experiment[29].

In regard of this, nano/micro structures might play a significant role in enhancing the surface wettability, by increasing the high capillary wicking. In this work, Si randomly nanowires were chosen as super-hydrophilic nanostructures since the fabrication method is easy, scalable and not expensive[11] The measurement of the wettability is usually performed by computing the apparent contact angle of a sessile droplet spreading on a surface. This way of assessing the wettability does not properly quantifies the *dynamics* of a droplet spreading, which should be coupled by assessing the wickability[30].

In fact, the effect of the wicking on micro/nano structures has been studied in many works in the previous years, but various techniques have been developed to evaluate the wicking performance. To accurately characterize the wicking of the nanowires, a literature review of the wicking metric was performed.

The most common methods are the *vertical strip test* feeded by an unlimited source (becker with liquid), *the spot test* feeded by a droplet (limited source), or by an unlimited source that can provide a continuos feeding(capillary tube)[31].

A good comparison between *the vertical strip* test and *the spot test* with unlimited source was found by Harnett and Mehta[32], but not the same between the spots with limited and unlimited source. It might imply the existence of a correlation between the wicking behavior and the size of the wicking feed. Therefore, the choice of characterizing the wickability cannot be neglectable before studying a specific phenomenon such as Pool Boiling or Leidenfrost effect, which respectively have an opposite behaviour.

Previous studies have focused mostly on the first two stages, because the time scale phenomena of boiling and wicking is short. Furthermore, experiments have shown that wicking in these first two stages obey the dynamic scaling law $r \; \alpha \; t^{\frac{n}{2}}$. Some have also reported the wicking coefficient[33], computed as the slope of the wicking lenght (shown in Figure 2.3), defined as the difference between the precursor ring and the contact line, versus the square root of the time. However, this is not properly correct since the trend of the curve is not perfectly linear.

Since in this work it is proposed a synchronized measurement for the wettability and wicking on different nanowires samples, a focused review on a wide range of nanostructures has been made.

In 2007 Fan et al. studied the spreading of a water drop on vertically aligned Si nanowires having different heights[34], with particular attention to the second stage. They found the n to be not affected by the height, and also comparable with a rough and porous surface(with respectively n=0.3 and n=0.25). Finally they found the n of the wicking lenght to be 1, according to the Washburn's law, $r \; \alpha \; t^{\frac{1}{2}}$ [35].

In 2012 Ahn et al. investigated the wicking on a zircaloy surface covered by nanotubes[1]. They found a monotonic linear increasing function in the first stage, while in the second stage an $n_c = 0.118$ and $n_p = 0.265$ for respectively the contact line and the precursor ring.

In the same year(2012) Mai et al. studied the vertical wicking of water and oil droplets impinged upon silicon nanopillars of different height. They showed that wicking can be tuned by varying the geometry[36]. A maximum

velocity was found by increasing the height, which probably caused a raise in terms of viscous forces.

Kim et al.(2014) studied the effect of the diameter on the wicking by considering patterned Si nanowires with same height and pitch[33]. Surfaces with smallest nanopillars diameter showed the highest wicking coefficient, equal to 1.28 $mm/s^{0.5}$. The lower is the pitch, the higher should be the capillary radial force during a droplet spreading.

After two years(2016), the same authors investigated the second stage of wicking on Si random nanopillars. In this case they focused more on the effect of the nanowires height, and they also considered two fluids(DI water and FC-72)[29]. By varying height did not affect the behaviour of FC-72, which has not shown any spreading. Different is the case of DI water, which enhanced the hemi-wicking stage as the height increased. This work suggests that wicking might depend on the fluid properties. A low surface tension[37], like in FC-72, could explain no wicking effect, whatever the surface is.

In 2017, Chen et al. investigated the wicking effect on ZnO nanowires samples. They fabricated random structures by the hydrothermal synthesis method. These surfaces presented a different morphology, a regular and an irregular array[2]. The regular surfaces showed a lower spreading and wicking than the irregular ones. Generally, small nano-channels increase both the capillary and viscous forces. The irregular surface have a multiscale nano-channel size distribution, which probably gives a better balance in terms of the mentioned forces respect to the regular array structures. Furthermore, for a specific array, the nanowires with the medium height have shown the highest wicking rate. This can be attributed again to the balance previously mentioned.

In 2017, Shim et al. computed the wicking lenght for random and triangular aligned silicon nanopillars[28]. They also investigated different heights, and for both the cases an higher height led to an higher wicking co-efficient. Anyway, the best wicking performance was reached by the arranged structures, whose the morphology suits better for a less flow resistance than the random structures. These lasts show entanglments between nanowires, which considerably increases the solid fraction.

Wemp et al.(2017) introduced a predictive model for the syncronous and hemi spreading stage. They verified it on experimental data of water droplets spreaded on random ZnO nanowires, which were thermally fabricated on a

copper substrate[19].

Many efforts have been employed so far, but there is no a general method which fully depicts the wicking properties of the different surfaces. This led to many parameters, which make the surfaces uncomparable and also the predictive models not suitable for describing a certain phenomenon.

In other works[33, 36], the wicking was studied by vertically dipping down the sample in a filled becker. Some others placed a filled capillary tube in touch with a surface, and measured the volume flux involved in the wicking by tracking the movement of the meniscus in the tube[38, 30]. Although it is a simple approach, it does not allow to catch the contact line, precursor rim and the wicking length, which instead could be tracked by a top camera. Infact, the evaporation of a droplet on a porous surface would require to track the heat exchange area, which is clearly linked to the precursor rim[26].

However, most of the authors[34, 1, 2, 39] have studied the wicking by impinging a droplet upon a horizontal surface , but they measured the wicking characteristics by only considering one radial direction during the droplet spreading. Fan et al.[34] and Kim et al.[33] considered more than one measurement. They respectively have taken into consideration two perpendicular and octangular radial directions. Only Wemp et al.[19] were able to derive the mean radius by measuring the wetted area (through ImageJ), which corresponds to consider all the directions.

Our method is applied on random silicon nanowires structures, which have already shown a really great performance in droplet cooling[11], pool boiling[40] and flow boiling[7, 41].

About the first one, Shim et al.(2017) reported only the wicking lenght (hemispreading stage) against the square root of time of a water droplet impinged on random silicon nanopillars. They only limited to compute the wicking coefficient for three samples with three different heights(h $= 2, 5, 7$ μm). The values reported were respectively w $= 0.31, 0.40, 0.43$ mm/s$^{0.5}$[28]. On the contrary, the power law coefficient of the precursor rim and contact line were not computed.

Hsieh et al.(2005) only reported the effect of the wicking on the droplet cooling over a micropillars surface in terms of evaporation time, but no assesment of the wicking is present[42].

About the pool boiling, Rahman et al.(2014) used a capillary tube, and computed experimentally a phenomenological parameter which takes into account the initial volume flux and the initial prewetted Area. They respectively take into account the contact angle and the wickability. Hovewer, in this case the source is continuos, and the method is not able to catch the precursor ring, whose the area is necessary for the efficiency of heat transfer[27].

Regarding to the flow boiling experiment, Kim et al.(2016) carried out the Kim et al.(2016) carried out the vertical strip test feeded by becker with water (unlimited source). They did use of random and patterned silicon nanowires, and they just showed how the wicking lenght changes with the height (h = 2.5, 6.8, 15.8 μm)[29]. The increase of the wicking with the height is probably due to the collapsing of the same nanowires, which after a certain height bundle and create wide distributed cavities with size various micrometers[43]. This configuration seems to the most adaptable to not obstruct the flow.

Among all the works reported so far, no one has carried out a fully synchronized characterization of wettability and wicking for super-hydrophilic surfaces. Wettability and wickability are supplementary for a full description of a super-hydrophilic surface[30]. Furthermore, the measurement of apparent contact angle, contact line and droplet volume can be taken into account for the benchmark of some theoretical predictive models for the droplet evaporation[44].

For example, the case could be a droplet impinged on a random nanowire strate. By knowing the volume of the impinged droplet and of the upper droplet(which require the contact angle and contact line), it is possible to compute the volume inside the randon nanowires.

A synchronized and valid method of wettability and wickability characterization for super-hydrophilic surfaces is then proposed in this thesis. In order to perform a detailed tracking transient evolution of wettability and wickability, different in-house Matlab codes have been built.

Two high speed cameras have been synchronized in order to catch the simultaneous evolution of the contact angle and prewetted area of a droplet impinged on the surface. A front camera is used for the contact angle, while a top camera is in charge for the other task. In fact, the front camera is not able to catch the precursor rim, cause it diffuses inside the micro/nano

wires strate. Further, real surfaces do not show an uniform spreading of the upper droplet and the precursor rim. Therefore, a top camera is necessary to exactly detect the wetted areas(and so the equivalent radius).

In this regard, this work aims to investigate the effect of the wickability on the droplet evaporation on Si random nanowires. In order to assess the role of the wicking on the evaporation, three different samples with three different heights were fabricated. Two validated Matlab codes were developed, optimized and validated in order to track the contact angle evolution and measure the spreading area of the droplet. After a systematic characterization, the heat transfer experiments were performed.

Chapter 3

Design of the wicking facility, validation and development of the Matlab codes

3.1 Experimental setup and procedure

The design used for the experiments is shown in the Figure 3.1. Two high speed cameras were synchronized in order to catch the simultaneous evolution of the spreading (top camera, FASTCAM Mini UX100) and of the contact angle (front camera, FASTCAM SA3 Model). Two lights were installed in order to improve the visualization of the cameras. The models used were a OSL2 Fiber Illuminator and a Cold White Mounted High-Power LED. The levelling stage allows to align the sample horizontally.

Since it is important to keep the volume droplet in a narrow range, a microsyringe electric pump was used . The distance between the needle and the sample was set such as the water droplet is released due to the capillary effect of the nanopillars. Therefore, the needle is located very close to the surface. By setting in the pump a flow rate of 0.03 ml/min and a volume of 5 μl, it is possible to get the volume of a water droplet varying from 4.2 to 6 μl. This has been verified through the image processing, and after a suitable calibration between pixel and millimiters, whose more details follow.

The videos were started manually by the means of an external trigger,

through it has been possible to record prior the droplet touches the surface. Then, the initial time t = 0 is chosen on the frame when the droplet touches the surface. The frame rate chosen was 500 fps, therefore the systematic uncertainty coming from an instant time is the reciprocal of the frame rate.
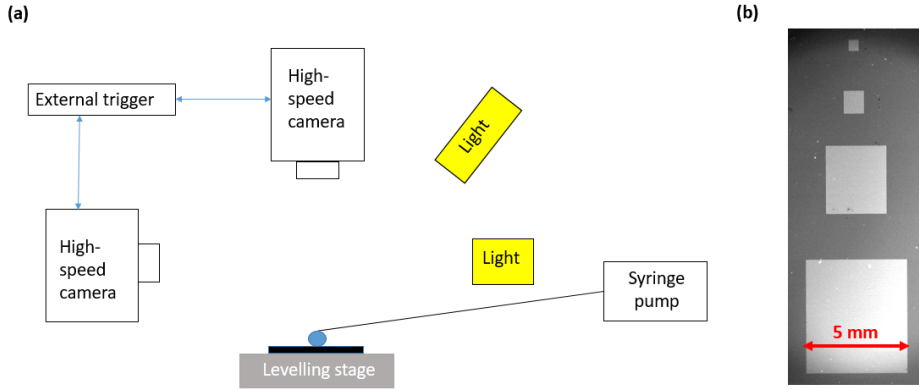

Figure 3.1: (a)Design of wicking facility (b) Calibration tool

Since the wicking is a phenomenon which occurs at very low space and time scale, it is important to be accurate as much as possible. A very precise tool was made by the means of lithography for the calibration. The tools involved were MLA150 Maskless aligner, AJA Sputter and Evaporator, Field Emmision scanning electron microscope (SEM). Five squares of different sizes were created on a silicon sample. Figure 3.1 shows the first four squares of this tool. The design lithography values were supposed to be 0.5, 1.0, 3.0, 5.0 and 15.0 mm; this range suits adaptable for our range of interest. Anyway, the supposed values have to be replaced by what measured in SEM, which is a very accurate optical instrument of measuring. By considering the mean for each set of measurements of the squares, the real sizes of the squares are 0.49, 0.99, 2.98, 4.96 and 14.89 mm. These sizes are then considered the true values (or weights) for the calibration curve, which is supposed to linearly relate the pixels and the millimeters. An in-house Matlab code was developed in order to achieve the pixel value of the size squares. It is able to detect the boundaries of the object, as shown in Figure 3.2.

32
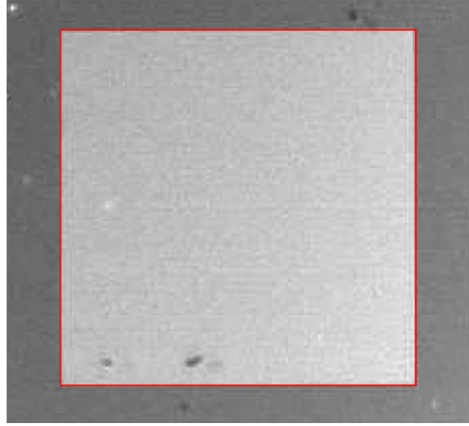
Figure 3.2: Square catched with red lines by the Matlab code

For each square, four measurements of the side were performed. The calibration curve is then obtained by a linear regression fit as shown in Figure 3.3.
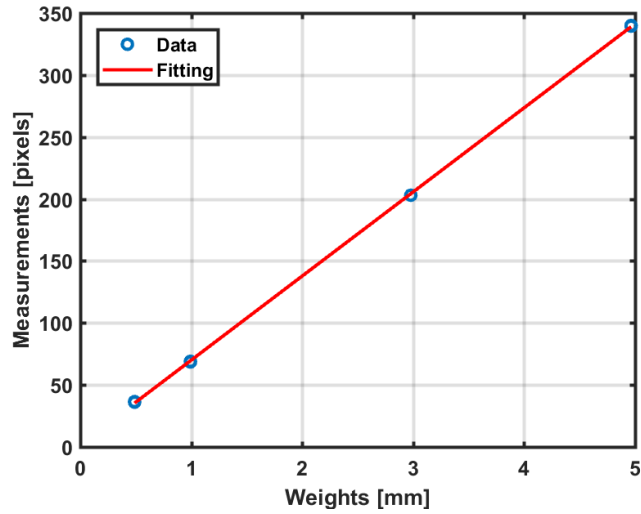
Figure 3.3: Calibration curve

At the same way, the code further developed in order to catch the boundaries of the contact line and the precursor rim, as shown in Figure 3.4.
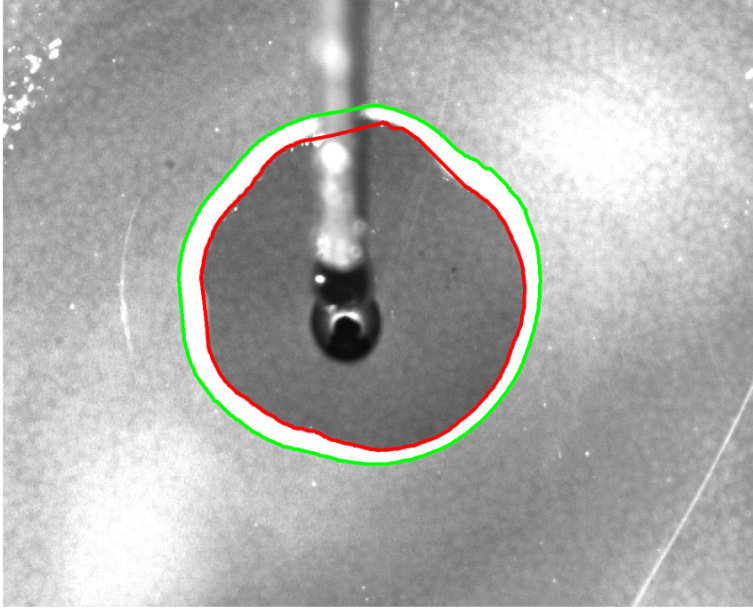
Figure 3.4: Calibration curve

Further details of the code are the described in the next section.

3.2 Results

3.2.1 Development and validation of the wicking code

A basic written Matlab code has been improved and optimized in order to catch the contact line and the precursor rim during the spreading phase. This code has been validated before to be applied on the droplet case.

3.2.2 Vertical/Horizontal strip test validation

The first step of the validation was to achieve the wicking velocity of the water in the uniform porous paper provided by the General Electric Health-Care, in particular a Grade 3 Chr Cellulose Chromatography; the last step was to compare our value with the one computed by the GE, which have only considered the vertical case. At least five measurements of wicking for the horizontal and vertical case were performed, and an error analysis has been carried out.

The experimental setup consists of a becker filled up with DI water and some pieces of the GE paper, standardized by the same dimensions (width = 2 cm, length = 8 cm). These lasts are the same for the two cases, and were chosen by making some pratical considerations. Two tips could be considered for this choice:

- The width has to be long enough that the paper could be catched in the camera;

- The length has to be such as it can stay as stiff as possible during the experiment and also enough that the wicking can be recorded once the water has crossed a proper distance from the becker;

A long paper can be more affected by bends during the crossing front of water, and a recording video that occurs when the water front is still nearly to the becker could be considered an unsteady regime for the wicking phenomenon. In fact, the becker could be considered an "infinite source" compared to the amount of liquid that is wetting the paper, and the effects of pumping the water are visibly enhanced when the paper just touches the water surface. An example of frame is shown in Figure 3.5.

35

Figure 3.5: Crossing of the water through the GE paper

The reference of start for the time and the distance is chosen in the first frame of recording (frame rate = 50 fps). At this frame, it is imposed a time $t_0 = 0$ s and a distance $D_0 = 0$ mm; Two approaches were considered to catch the distance crossed by the water in the paper, a *Point Approach* and an *Area Approach*. The first consists of in the tracking of a point in the water front, where the distance is easily computed by taking the distance of the point with respect to the basis, while the second in the tracking of area front, where the distance is computed by dividing the area for the width of the wetted region. The final graph distance versus time arises a linear trend, and the two approaches are compared on the same graph, as reported in the Figure 3.6, which clearly highlights that the Area approach is the best choice for its linearity.
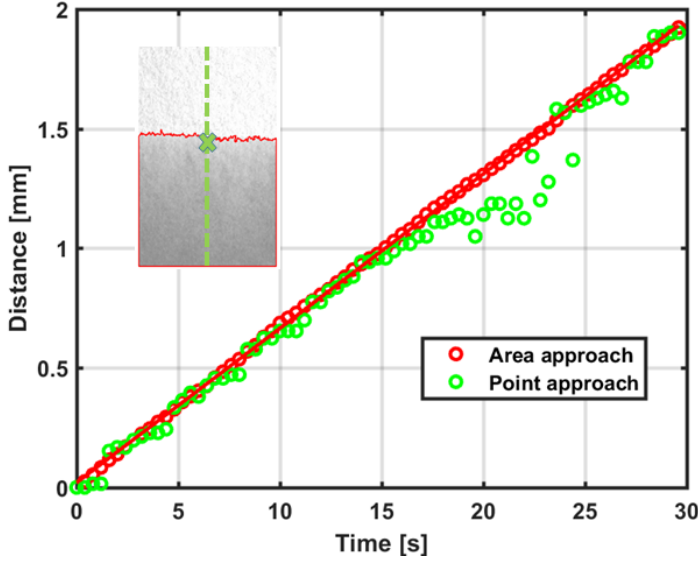
Figure 3.6: Distance vs Time in the vertical strip case

Furthermore, the Area Approach acts to reduce the noise generated by the image processing. It takes into consideration an average of all the points located at the front. The same method was considered for the horizontal case. Since the velocity is computed on the linear fit, its expression can be explicated as:

$$v = \frac{D_{end} - D_0}{t_{end} - t_0};$$ (3.1)

where *end* is referred to the last frame recorded, and *0* is referred to the first frame recorded. The final values for the vertical and horizontal case were respecitvely 0.065± 0.003 mm/s and 0.063 ± 0.004 mm/s. The results are very close to each other, this might imply that gravity does not play a significant role in the vertical wicking. However, the results show a maximum difference of approximately 9 % respect to the value provided by GE (0.071 mm/s). Therefore, the method can be considered validated.

37

3.2.3   Spot Test - Droplet case

The droplet spreading on the same GE paper was considered. The Radius versus Time graph in Figure 3.7 highlights a non linear relation.
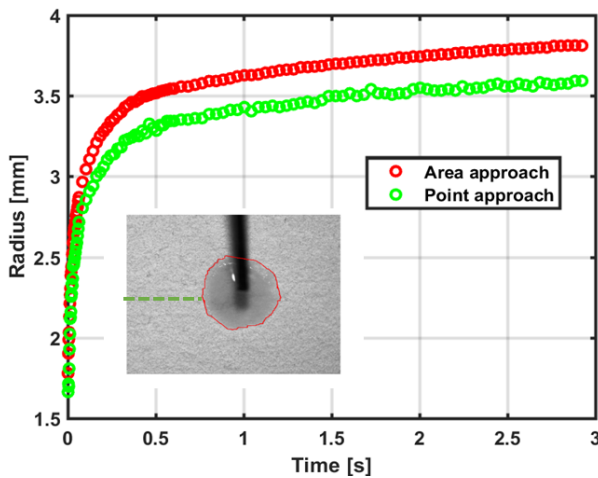

Figure 3.7: Distance vs Time in the spot test

Also in this case is possible to remark the better approach given by catching the wetted area. The red curve, which is more accurate than the green curve, does not show significant fluctuations. Finally, a comparison between the spot test and the previous tests can be made, as reported in Figure 3.8.
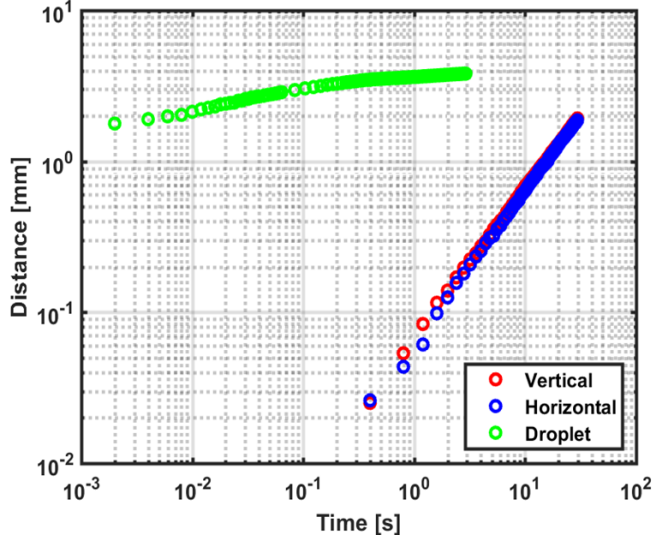
Figure 3.8: Comparison between vertical strip, horizontal strip and spot test

Since the Wicking in a porous media obeys the dynamic scaling law r α t$^{\frac{n}{2}}$, it is worth to compute the n coefficient to quantitatively assess a comparison between these cases. As it is mostly done in the literature, the n coefficient for a droplet is computed in the hemi-spreading stage (II stage), which is the predominant phase of the wicking phenomenon. Therefore, the n power law coefficient was computed as:

$$n = 2 * \frac{\log(r_{end}) - log(r_1)}{log(t_{end}) - log(t_1)} \quad (3.2)$$

In the case of vertical/horizontal case the n is computed just replacing the radius with the crossed distance D.

Table 3.1 summarizes all the n computed for the different cases.

Table 3.1: Comparison between the different wicking cases for the GE paper (area approach)

	Vertical	Horizontal	Droplet
n [-]	1.99 ± 0.10	2.00 ± 0.04	0.27 ± 0.02

As expected, the vertical and horizontal cases have an n similar to 2, which means a linear behaviour. The droplet case has a much lower n. It might be attributed to the different source, in this case limited to a droplet.

3.2.4 Sensitivity analysis

A sensitivity analysis was implemented in Matlab to catch the most appropriate values that are most suitable for the image processing. This algorithm has the same approach of the Bisection method, cause it spans more intensity pixel Levels and Remove Pixel intervals. Through this analysis it is possible to get the level interval of interest in a very fast and easy way; By looking at the boundaries enclosing the object and at the range where the radius droplet does not vary significantly, you can reduce whatever you want the interval of intensity level. This allows to achieve a precise level that well identifies the object boundaries. After a level sensitivity analysis, the same algorithm is applied on the Remove Pixel interval, which allows to remove all the circles and holes that are close your interested Area. Figure 3.9 represents 3 subsequent images altered by the processing image, in the case of Vertical/Horizontal strip case. They tadily represent the original image on the left, which is firstly subjected to a Level sensitivity analysis, and then to a Remove Pixel sensitivity analysis.
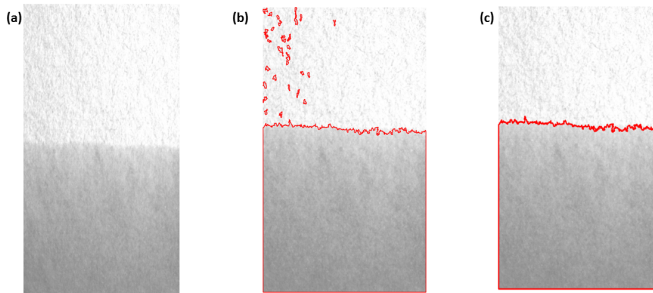

Figure 3.9: (a) Original image (b) Altered Image after a Level sensitivity (c) Altered Image after a Remove Pixel sensitivity

Figure 3.10(a) shows the the effect of the Level and of the Remove pixel

on the droplet radius. In such a case, it is interesting to notice that the droplet is enclosed by boundaries in the range going from 0.60 and 0.70, as highlighten in the subset images. Furthermore, a not significant variance of the radius is observed in the 0.65-0.70 Level range, which ensures a reliable value of the radius. The Level sensitivity analysis was performed with a fixed Remove Pixel value greater than 200, which ensures no noise in the calculation of the radius, as shown in the same Figure 3.10(b).
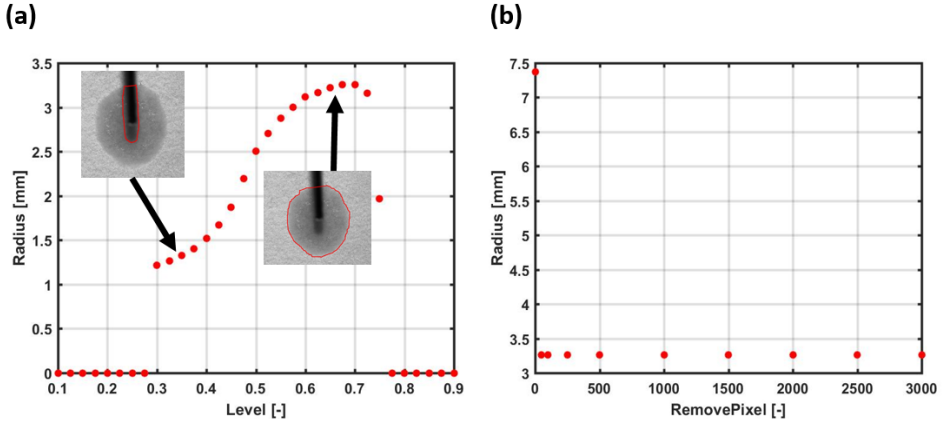
Figure 3.10: (a) Effect Level on the Radius droplet (b) Effect Remove Pixel on the Radius droplet

3.2.5 Development of contact angle code

A contact angle code was developed in order to compute the apparent contact angle during the spreading of the droplet. Based on the same approach previously descripted, the method was validated by comparing the values of a contact angle of a DI water droplet impinged on plain Si surface. Figure 3.11 points out the difference between the two values given by the Matlab code and the tensiometer.

41
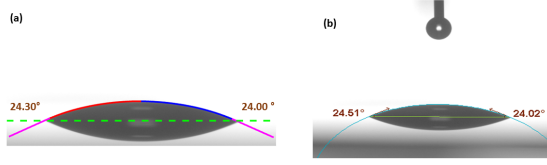
Figure 3.11: (a)In-house Matlab code,$CA_{left}=24.30°$ $CA_{right}=24.00°$ (b)One Attension Tensiometer, $CA_{left}=24.51°$ $CA_{right}=24.02°$

The In-house Matlab(values in Figure 3.11 (a)) code presents a maximum difference of only 0.86 % with respect to the tensiometer(values in Figure 3.11 (b)). Moreover, the code is based on taking the polynomial fit of half air - droplet interface. By computing the first derivative in zero, it is possible to get the slope of the tangent, which is easily related to the contact angle. Figure 3.12 shows an example of a fifth order polynomial fit on one of the frames analyzed during the data processing of one sample.

Figure 3.12: (a)Polynomial fit of experimental data, CA_{left} (b)Polynomial fit of experimental data, CA_{right}

The choiche of the polynomial order was made after verified the highest *Adjusted* coefficient of determination R^2[45]. That was verified for different frames during the evolution of the contact angle over the 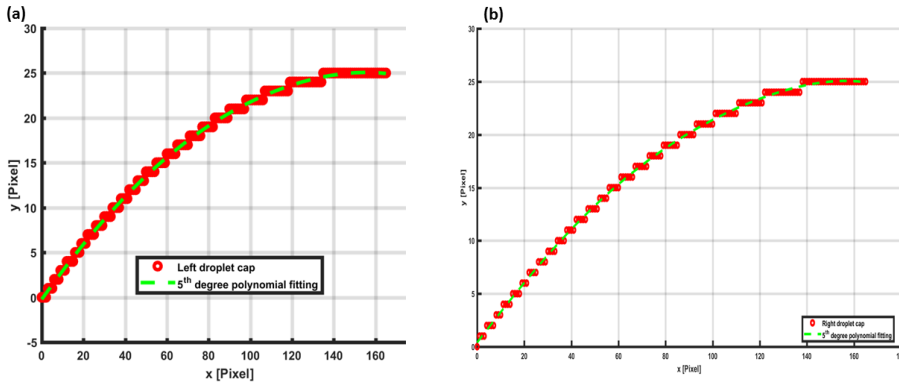time. The orders considered were 2,3,4,5. Figure 3.13 sums up all the Adjusted R for the left and right contact angle for different instant times. It is clear that the order five results to be the best polynomial fit for half of the air-droplet interface.
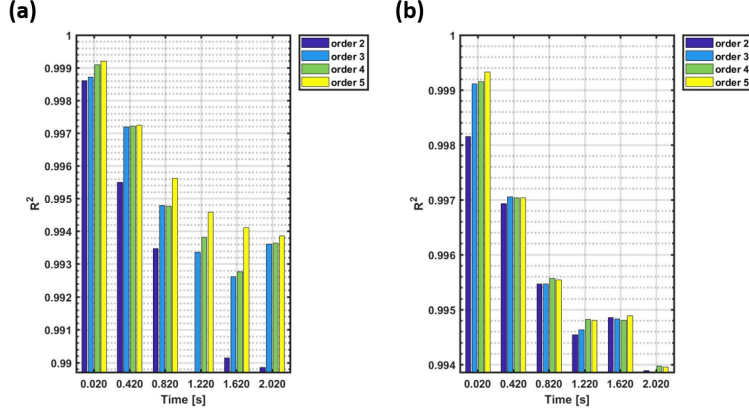
Figure 3.13: (a) R^2 adjusted for different frames, CA_{left} (b)R^2 adjusted for different frames, CA_{right}

3.2.6 Experimental uncertainty

Total uncertainty of a measurement is given by the contribution of a systematic and random uncertainty. Therefore, it can be computed by referring to the square root of the sum of the squares[46]. The final equation is:

$$W = \sqrt{B^2 + P^2} \tag{3.3}$$

where B is the systematic uncertainty and P is the random uncertainty. Total systematic uncertainty is computed by averaging the systematic errors coming from the set of measurements. Random uncertainty is computed by taking into account the t-distribution with a confidence level of 95%, that is given by:

$$P = t_{distr} * \frac{S}{N} \qquad\qquad (3.4)$$

where t_{distr} corresponds to the value from the t-distribution, S is the standard deviation from the N measurements considered.

Calibration uncertainty

The final calibration error, which is systematic, is computed by taking into account the non linearity, accuracy and repeteability errors[46]. To estimate the accuracy, the maximum deviation from the zero value (given by the linear fit of the calibration curve) was taken, which gave the accuracy limits. Figure 3.14 shows all the deviations from the linear fit. For the nonlinearity evaluation one can average all the deviations that were taken for each square, which is plotted as the blue dots in Figure 3.14. The red line in the figure connects the terminal points of the data, while the green line shows the evaluation of the terminal linearity as the maximum difference between the average point and the red line.
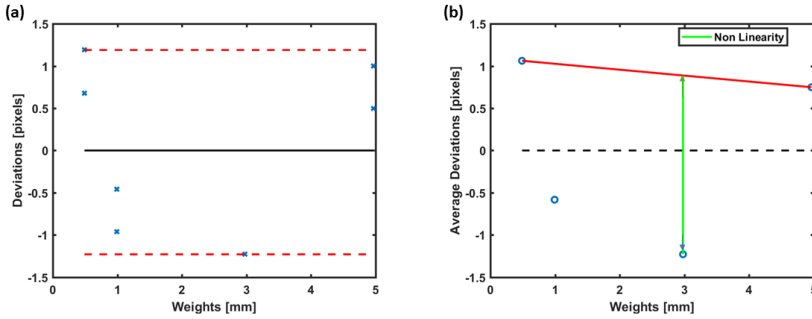

Figure 3.14: (a) Accuracy error (b) Non-linearity

The error due to repeatability was found by computing the highest

variability for each square considered. By taking the maximum among this values is possible to quantify the repeatibiliy uncertainty[46]. Finally, the total systematic uncertainty due to the calibration is:

$$B_{cal} = \sqrt{B_{nl}^2 + B_{acc}^2 + B_{rep}^2} \qquad (3.5)$$

Vertical/Horizontal strip test

The velocity is computed according to the equation 3.1, as discussed before. Then the RSS[46] is applied to combine the systematic uncertainties on space and time, by giving:

$$B_v = \sqrt{(2\frac{2B_{cal}}{\Delta t})^2 + (2\frac{B_t}{\Delta t^2}\Delta D)^2} \qquad (3.6)$$

where ΔD is the distance crossed by the wicking front in the time interval Δt, and B_t is the systematic uncertainty on the time, given by:

$$B_t = \frac{1}{fps} \qquad (3.7)$$

Spot Test

As previously discussed, the power law coefficient is representative of the wicking phenomenon. It is computed according to the equation 3.2. The systematic uncertainty is again computed by applying the RSS. For a single measurement, the systematic error is:

$$B_n = \sqrt{(2 \quad \frac{B_{log_r}}{\Delta log_t})^2 + (\frac{2B_{log_t}}{(\Delta log_t)^2} \quad \Delta log_r)^2} \qquad (3.8)$$

where

$$B_{log_r} = B_{cal} \quad (\frac{1}{r_{end}} \quad \frac{1}{ln(10)} + \frac{1}{r_1} \quad \frac{1}{ln(10)}) \qquad (3.9)$$

45

$$B_{log_t} = B_t \quad (\frac{1}{t_{end}} \quad \frac{1}{ln(10)} + \frac{1}{t_1} \quad \frac{1}{ln(10)}) \tag{3.10}$$

$$\Delta log_r = log(r_{end}) - log(r_1) \tag{3.11}$$

$$\Delta log_t = log(t_{end}) - log(t_1) \tag{3.12}$$

Wicking coefficient

The wicking coefficient w is obtained by computing the slope of the linear fit of the curve that relates the wicking length to the square root of the time. As said before, the wicking length l is defined as the difference between the precursor rim r_p and the contact line r_c. Then the wicking coefficient can be defined as :

$$w = \frac{l_{end} - l_0}{\sqrt{t_{end}} - \sqrt{t_0}}; \tag{3.13}$$

The systematic uncertainty for a single measurement is again computed by applying the RSS.

$$B_w = \sqrt{(2 \quad \frac{2 * B_{cal}}{\Delta\sqrt{t}})^2 + (\frac{2B_{\sqrt{t}}}{(\Delta\sqrt{t})^2} \quad \Delta l)^2} \tag{3.14}$$

where

$$B_{\sqrt{t}} = B_t \quad (\frac{0.5}{\sqrt{t_{end}}} + \frac{0.5}{\sqrt{t_1}}) \tag{3.15}$$

$$\Delta l = l_{end} - l_1 \tag{3.16}$$

$$\Delta\sqrt{t} = \sqrt{t_{end}} - \sqrt{t_1} \tag{3.17}$$

Chapter 4

Wicking on random Si nanowires

Recent research showed that is possible to control the heat transfer performance when a droplet is impinged on a surface. This can be achieved by tuning the wettability and surface roughness. In this regard, a significant role is played by micro-nano structures[11]. In this work, it is shown that it is possible to control the droplet cooling by increasing the wickability of the surface. For this study, three different random nanowires with three different heights were fabricated and characterized .

4.1   Fabrication and characterization

The fabrication requires two-step Metal assisted chemical Etching steps, whose more details are available in the work of Auliano et al.(2018)[11].It is an easy method, which is also cheap and suitable for industrial applications.

Silicon polished wafers with a crystallographic orientation $<100>$ were used. They have p-type Boron doping, a resistivity of 0.01-0.02 Ω cm, and 2 in of diameter.

Firstly, a thick silver film of 25 nm is sputtered at 0.5 Å/s in an electron-beam evaporator(AJA International Inc.Custom ATC-2200V). Then the wafer is dipped in a solution of 0.2 M of H_2O_2 and 5.1 M of HF. Afterwards it is

rinsed with isoprophanol (IPA) and dried on a hot plate. In the final step a 9 M nitric acid solution is used to remove the silver dendrites.

The characterization was perfomed by the means of the SEM. A SEM top view and cross section for each sample is shown with different scales in the Figure 4.1 .
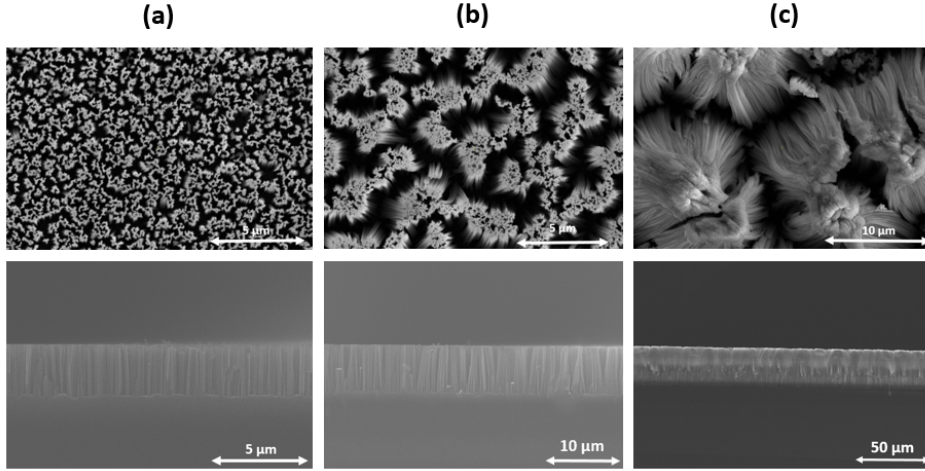

Figure 4.1: SEM top view(above) and cross section(below)(a) NW-A(d = 153 ± 9 nm, h = 2.51 ± 0.01 μm) (b) NW-B(d = 173 ± 8 nm, h = 6.32 ± 0.02 μm) (c) NW-C(d = 226 ± 25 nm, h = 25.27 ± 0.08 μm)

4.2   Wickability

The precursor rim coefficient n_p and the wicking coefficient w were computed respectively for all the samples. The radius of the contact line and the precursor rim were computed by dividing the square root of the wetted area and π [19]. Table 4.1 resumes the different heights of the named nanostructures.

Table 4.1: Heights for the different nanowires

	NW-A	NW-B	NW-C
h [μm]	2.51 ± 0.01	6.32 ± 0.02	25.27 ± 0.08

Figure 4.2 shows different synchronous snapshots of the top (wicking)

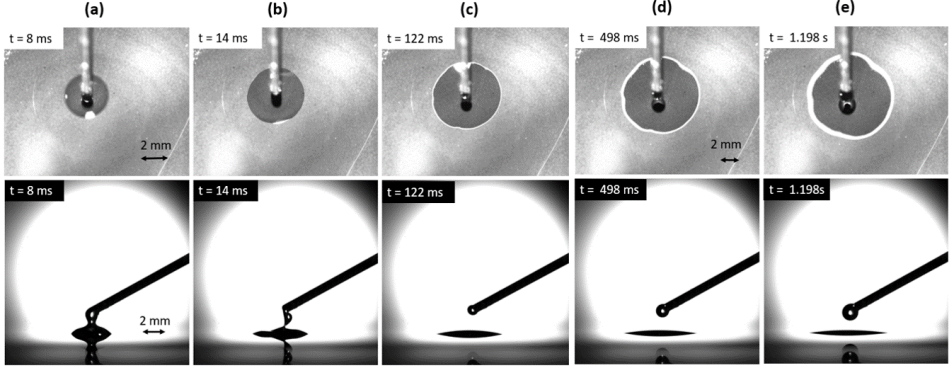and front camera (contact angle) of the sample NW-B.

Figure 4.2: Snapshots evolution of the wicking and spreading - NW-B

Figure 4.3 shows the radius of contact line and precursor rim and contact angle evolution for the one measurement of the NW-B.
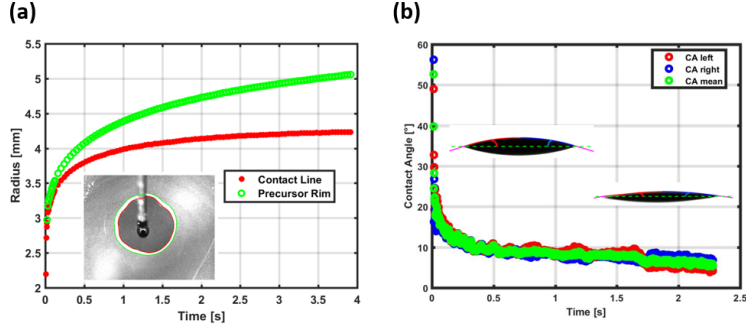
Figure 4.3: NW-B (a) Radius vs Time (b) Contact angle vs Time

As explained in section 2.3 the contact line and the precursor rim increase over the time. The contact angle shows a steep decrease in the first stage (syncronous spreading) followed by very low reduction in the second stage(hemi spreading). Figure 4.4 points out clearly the different stages in the loglog scale. It is interesting to notice that it was possible to identify a "third stage" for which the contact line is going to be reduced, that coincides with a lower slope than the hemispreading stage.

49

Figure 4.4: Radius vs Time in log-log scale - NW-B

To be complete, Figure 4.5 and Figure 4.6 report the same graphs for respectively NW-A and NW-C.
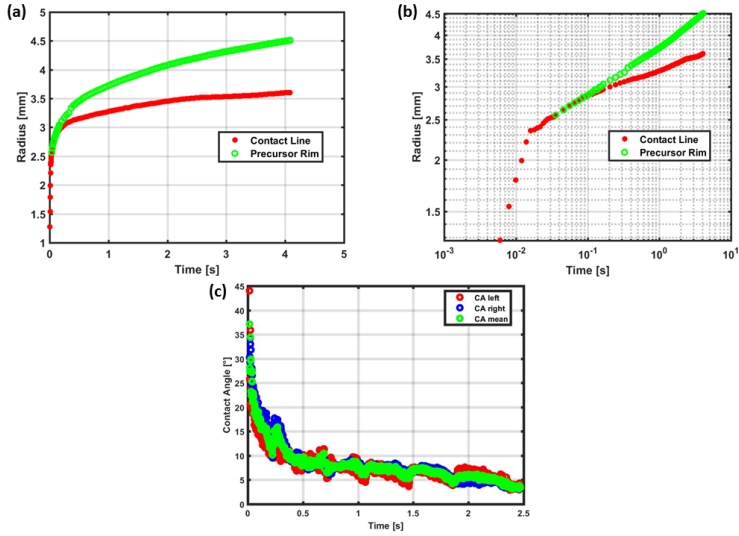
Figure 4.5: NW-A (a) Radius vs Time (b) Radius vs Time - loglog scale (c) Contact Angle vs Time
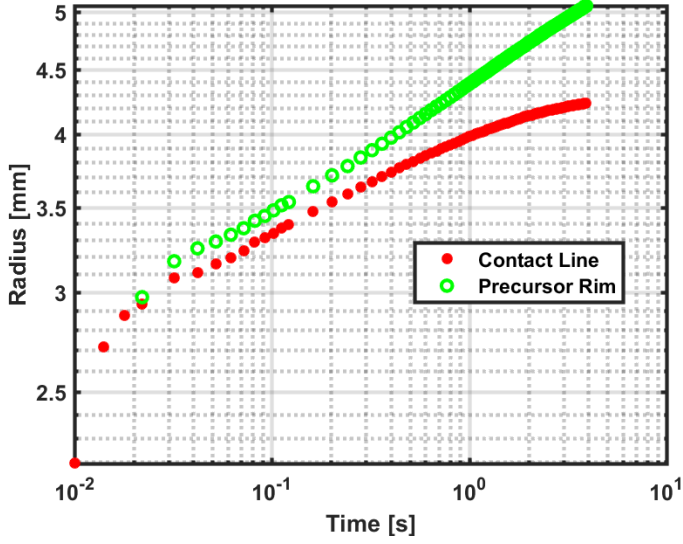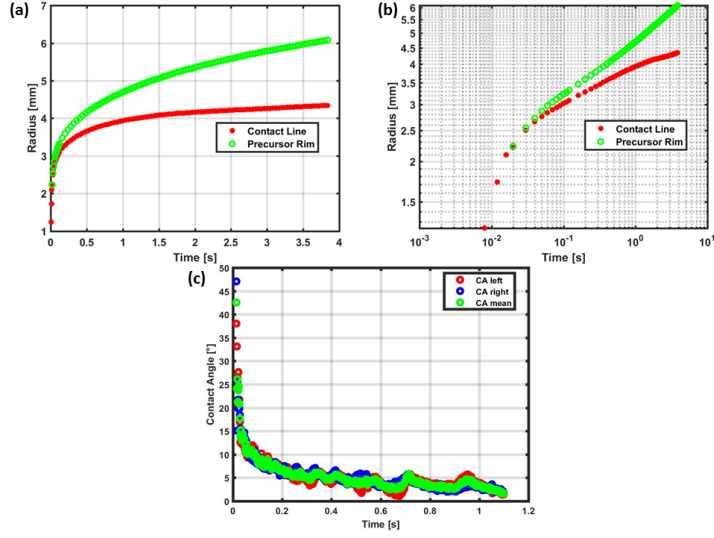
Figure 4.6: NW-C (a) Radius vs Time (b) Radius vs Time - loglog scale (c) Contact Angle vs Time

By looking at the log-log scale plot of the different nanowires, it is interesting to notice that the precursor rim spreads slower in the sample NW-A, which has the lowest height. Further, NW-A does not show a gradual transition between I and II stage compared to the other samples. On the contrary, in NW-C(with the highest height) the precursor rim spreads faster than the others by making the transition more continuos. Therefore, an higher height might imply an higher kinetic energy in the first stage, and consequently, an faster spreading also in the second stage.

4.3   Results and discussion

At least six measurements were considered for computing the n_p and the w coefficients. Table 4.2 sums up all the results for the nanostructures considered.

Table 4.2: np and w coefficients

	h [μm]	n_p [-]	w [mm/$s^{0.5}$]
NW-A	2.51 ± 0.01	0.21 ± 0.01	0.42 ± 0.04
NW-B	6.32 ± 0.02	0.25 ± 0.01	0.52 ± 0.05
NW-C	25.27 ± 0.08	0.35 ± 0.02	0.89 ± 0.08

It is interesting to investigate more on the effect of the height on the wicking, since the height is the only controllable parameter for these structures. Figure 4.7 makes a comparison between the nanowires about the spreading of the precursor rim.
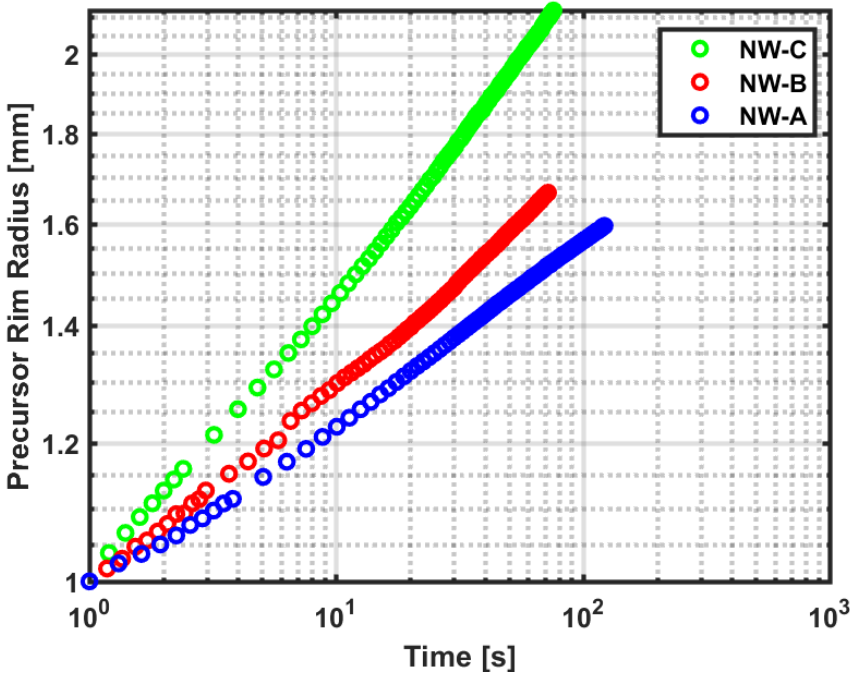

Figure 4.7: Comparison of the samples - Precursor rim versus Time (log-log scale).

The plot was made in loglog scale, then the initial time and initial radius of the precursor rim were translated in order to have a common reference for the space and time, and also to keep the n_p coefficient constant in the new reference system. The tallest nanowires (NW-C) show the highest slope,

which means the highest precursor rim coefficient. By considering the same approach, a comparison was made for the wicking lenght w, which is plotted versus the square root of time in a new reference system, as shown in Figure 4.8.
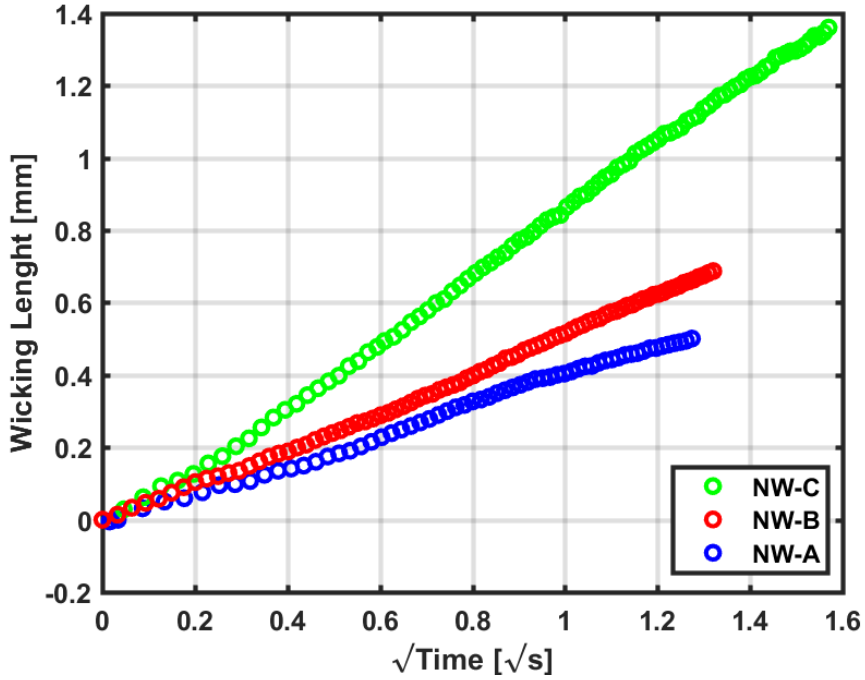

Figure 4.8: Comparison of the samples - Wicking lenght versus square root of time

Also in this case, the highest wicking coefficient was registered for the tallest nanowires. It has been shown that the higher are the nanowires, the higher are the two coefficients. Figure 4.9 makes a comparison in terms of contact angle.
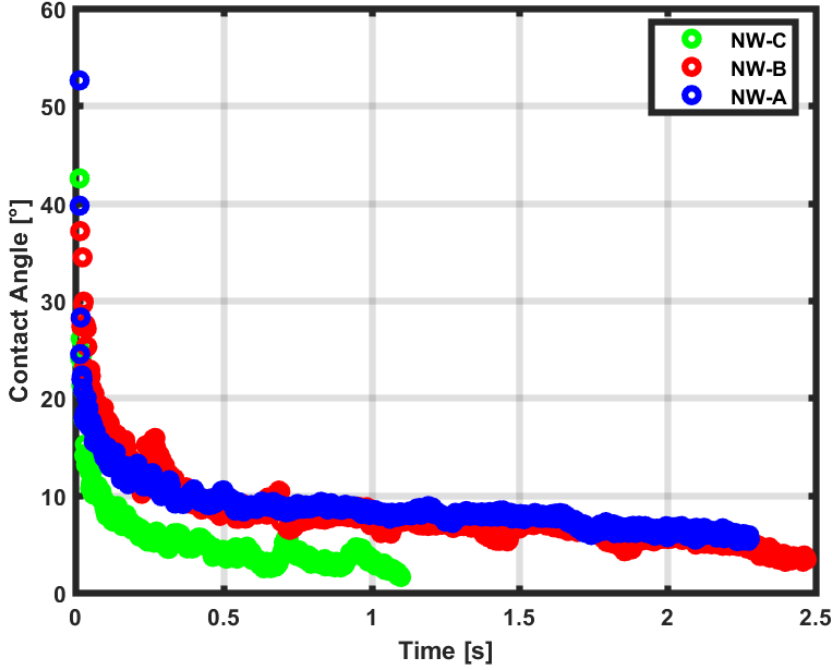
Figure 4.9: Comparison of the samples - Apparent contact angle versus Time

The highest nanowires have a very high decrease of the contact angle. The curve of NW-C is interrupted cause the contact angle code is not able to detect very low angles. According to the effect of the height on the wicking, the NW-B reaches a lower contact angle than the NW-A.

The effect of the height might be physically explained by the presence of two main forces, the capillary and the viscous forces[1]. When the space between pillars is reduced, the higher is the capillary pressure (inversely proportional to the pore radii) and the higher is the resistance due to the viscous forces. In this case bundling effect[11] of the pillars might play an important role. The higher are the pillars, the higher is the bundling effect, as it is shown in Figure 4.1. This causes a reduction in both the mentioned forces. Since the viscous force is opposite to the fluid motion, it should show an higher reduction respect to the capillary force.

4.3.1 Benchmark analysis

In 2017, Wemp et al. developed a theoretical model describing the wicking phenomenon in the first two stages[19]. The domain of interest is inside the nanowire strate. Due to the symmetry of geometry, boundary conditions and the driver(droplet), the problem can be reduced to 1D on the radial direction. A quasi-steady approach is considered. As the precursor rim spreads, the pressure field changes continuously to reach the equilibrium pressure field.

By considering an anular control volume for the precursor rim, the governing equations for both the two stage are the mass conservation and the Darcy's equation(Navier Stoke's equation applied for porous media). In the I stage, the upper droplet acts like an external source. A volumetric term is then inserted in the mass equation to take into account of the source. The final governing equation of the I stage is:

$$\frac{\partial^2 P}{\partial r^2} + \frac{1}{r} * (\frac{\partial P}{\partial r}) - \frac{2}{h^2} * (P - P_d) = 0 \tag{4.1}$$

The boundary conditions are :

$$\frac{\partial P}{\partial r} = 0 \ \ at \ \ r = 0 \tag{4.2}$$

$$P = P_a - \Delta P_{cap} \ \ at \ \ r = R \tag{4.3}$$

where P_d is the droplet pressure, which can be assumed equal to P_a(ambient pressure), and h is the average height of the nanowires.

For the II stage, the final governing equation is:

$$\frac{\partial^2 P}{\partial r^2} + \frac{1}{r} * (\frac{\partial P}{\partial r}) = 0 \tag{4.4}$$

where the boundary conditions are:

$$P = P_d \ \ at \ \ r = R_s \tag{4.5}$$

$$P = P_a - \Delta P_{cap} \ \ at \ \ r = R \tag{4.6}$$

where R_s is the radius of the precursor rim for which the hemi speading stage starts at the time instant t_s.

By integrating the equations, the two solving equations(that are referred to R_s and t_s) are:

$$r^* = t^* \qquad r^* \le 1 \tag{4.7}$$

$$\frac{r^*}{2}ln(r^*) - \frac{1}{4}(r^{*2} - 1) = \frac{h}{r_s}\frac{t^* - 1}{\sqrt{2}} \qquad r^* > 1 \tag{4.8}$$

This model has been experimentally verified on ZnO nanowires, whose the height varied from 3 to 5 μm. In this work, the model has been tried for the first time on Si random nanowires having a wider range of height. Before to assess the model on our sample, its applicability was verified. In fact, it can be applied only if the ratio between the upper droplet gravitational potential energy, kinetic energy and interfacial surface tension energy to the capillary pressure energy much lower than 1. This corresponds to approximately compute some dimensionless numbers, which respectively are the gravitational to surface tension force ratio $Bo = \frac{\rho_l\, g\, R^2}{h\, \Delta P_{cap}}$, the inertia to surface tension force ratio $We = \frac{R\, \rho_l\, v_d^2}{h\, \Delta P_{cap}}$ and droplet to capillary pressure ratio $Z = \frac{\sigma}{h\, \Delta P_{cap}}$. In our case, for all the samples the orders of magnitude were 10^{-6}, 10^{-6} and 10^{-2}. According to the authors of the model, the couple r_s and t_s was iteratively determined on the experimental data in order to best fit the experimental data. By looking at the Figure 4.10, the model seems to predict good the experimental data.
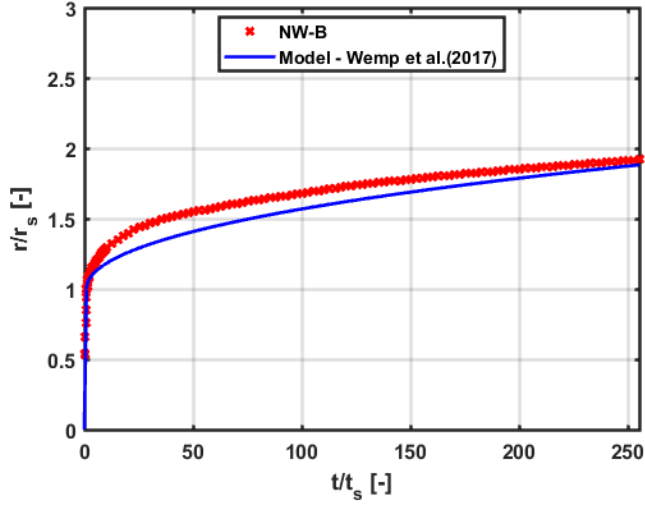
Figure 4.10: Comparison between model and NW-B, I and II stage

But zooming in the image for respectively the first and the second stage, the model shows some discrepancies with the experimental data, as shown in Figure 4.11.
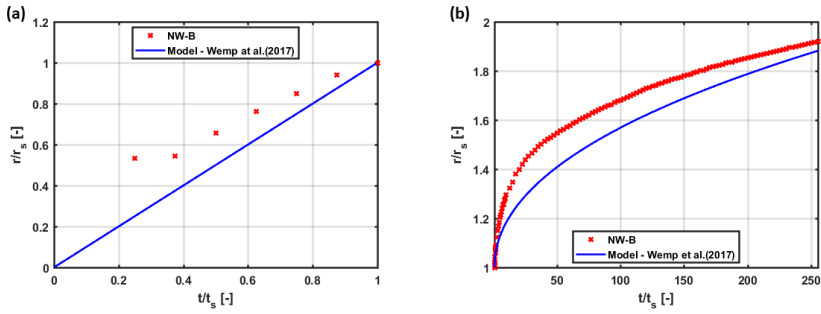

Figure 4.11: Comparison between model and NW-B (a) I stage (b) II stage

The first stage does not result properly linear, and the second stage differs from the model for a maximum of 15 %. The same has been reported for the others samples, as illustrated in Figure 4.12. Also here, the maximum differences with respect to the model in the second stage were respectively 18 % and 15 %.
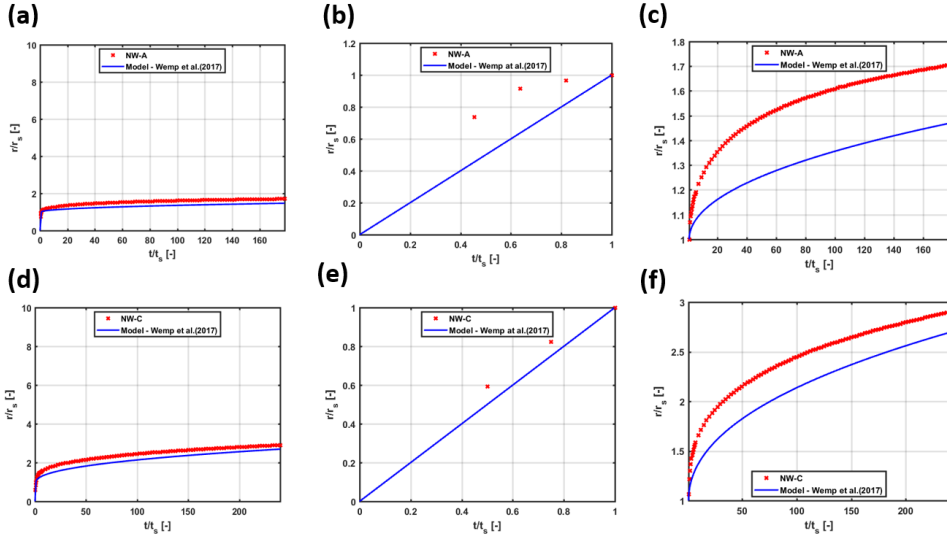
Figure 4.12: Comparison between model and NW-A and NW-C

According to Wemp et al.[19], the discrepancies can be attributed to the low porosity of the nano array, which would not be in agreement with the Darcy's model, or to the non uniformities, which would not be in accordance with the theoretical model.

Furthermore, the benchmark has been applied also for two other experimental works from Ahn et al.(2012) and Chen et al.(2017).The results are shown in Figure 4.13 and Figure 4.14, and also here the experimental data deviate from the model.
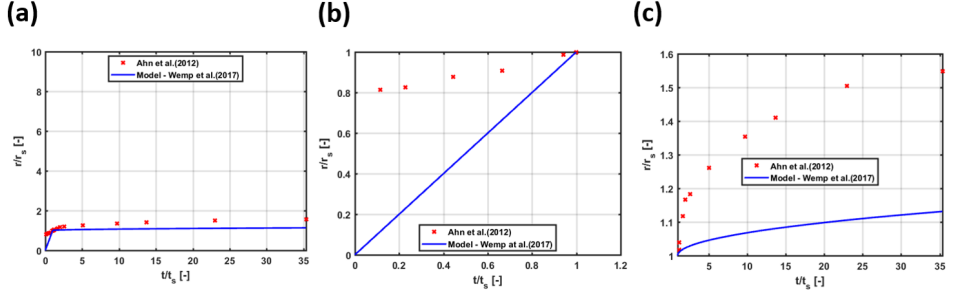
Figure 4.13: Comparison between model and Ahn et al. experimental data [1]
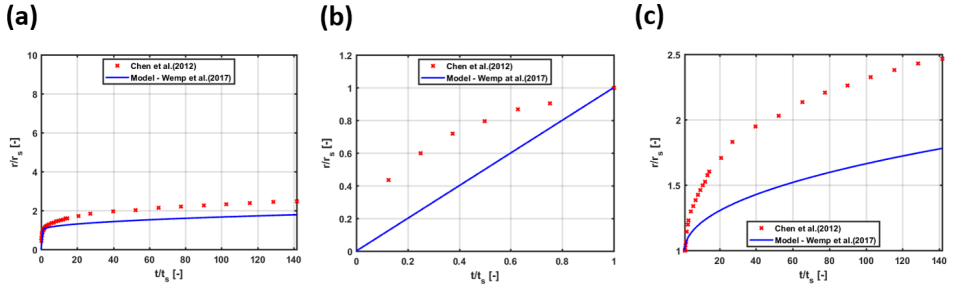
Figure 4.14: Comparison between model and Chen et al. experimental data [2]

The structures from Ahn are nanotubes, that are different from nanowires. A possible explanation could be that the hollow cylinder increase the capillary pressure from the top, which increases the spreading rate also in the second stage. In case of Chen et al., the deviation might be attributed to the non regular pattern of the random nanowires.

However, according to the hypothesis the model[19], it results to be more suitable for regular patterned structures, which will be analyzed in future works.

Chapter 5

Droplet evaporation on random Si nanowires

5.1 Description of the experimental setup

Figure 5.1 shows the evaporation experimental setup.

Figure 5.1: Design of the evaporation facility

It is un updated design respect to the previous one in Figure 3.1. The main parameters that describe the phenomenon are the time of evaporation, which is detected by the means of an high speed camera, and the temperature of the sample, that is detected by two K-type thermocouples fixed o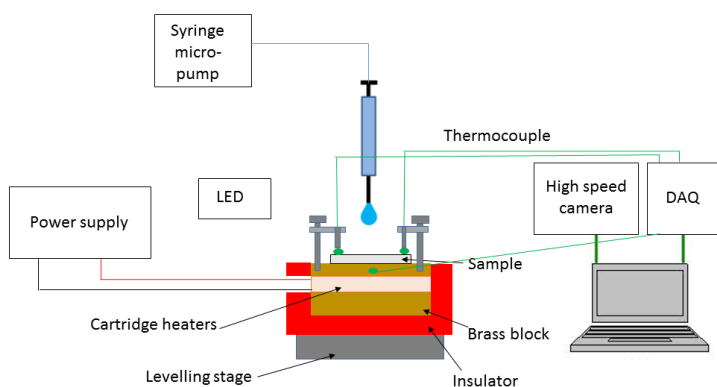n two opposite side of the sample. A thermal paste (OMEGA THERM 201) is required to reduce as much as possible the thermal interfacial resistance between the thermocouple and the sample.

The two temperatures are controlled by a power supply (Sorensen AME-TEK 100-15 DC), which is able to set a specific voltage. Four electric resistance are connected in parallel in the core of the brass block. The electrical circuit is closed by the power supply source. The Joule effect will convert electric power into heat. The brass block is surrounded by an insulation block (SFC - 2).

A third K-type thermocouple is inserted inside the block, just five millimeters below the sample. It is useful to detect the temperature of the brass for the regulation of the temperature surface. The temperatures of the three thermocouples are detected by a DAQ, which transfers the data to the computer for the processing.

As done for the wickability characterization, DI water droplets of the same size(about 5 μl) were considered. Due to the high surface temperatures, the droplets were impinged from an height of 5 mm with respect to the sample surfaces. Therefore, new parameters of the micro-pump were setted in order to keep the same range size of the droplets and to make the fall of the droplet caused only by gravity. Droplet diameter varies from 2.00 and 2.25 mm, which is smaller than the capillary length given by $Ca = \sqrt{\frac{\sigma}{\rho g}} = 2.7 \quad mm$. Thus, a droplet spherical shape is ensured before the impact on the surface.

For each temperature, at least four high speed videos of the droplet impinging on the surface were recorded. The video just starts when the droplet impacts on the silicon surface, and ends when it totally evaporates. The frame per second was chosen in order to reduce as much as possible the error on the time interval of evaporation. The higher is the frame per second chosen, the smaller is the error.

5.2   Calibration of the thermocouples

A calibration of the thermocouples was required before proceeding with the experiments. A proper oven (AMETEK RTC 700) was used to perform it. It is a very accurate instrument, which is able to reach stable temperatures in a range that goes from 30 to 700 °C.

The three thermocouples were placed inside the oven before starting the experiment. This allows to reach a thermal equilibrium between the themocouples (T_c) and the same oven . When the steady state is reached in the oven, four different sets of temperatures were detected. The measuring time for each set was one minute, and the interval time between two subsequent sets was one minute. Four values were derived by averaging over the measuring time. The same approach has been considered for the other T_{set}.

A calibration curve was finally obtained, and it is shown in Figure 5.2 for one of the thermocouples.
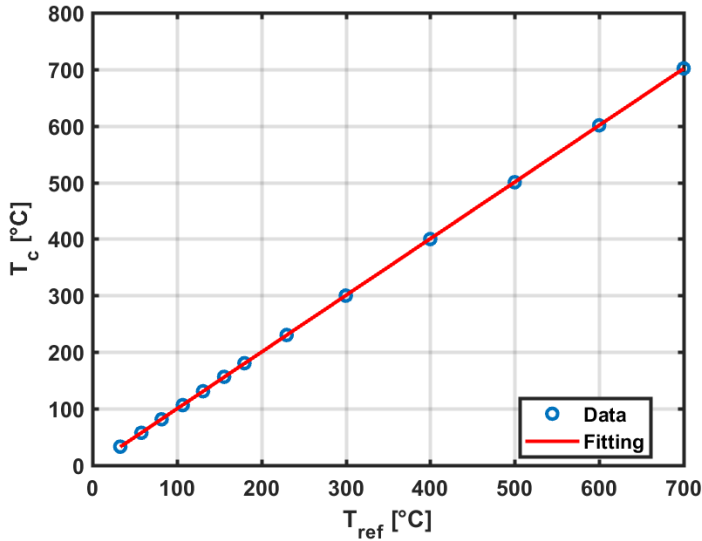

Figure 5.2: Calibration curve of one of the thermocouples

The curve is most refined in the range of the temperatures of our interest.

5.3   Validation of the facility

The facility was already validated in previous work [47, 16, 11], where a droplet volume of about 9 μl was used. Here, the droplet size was smaller(about 5 μl) than the previous case. Therefore, a new reference case was performed on a plain Si surface. Anyway, the case of 9 μl was repeated prior the case of 5 μl. The Leidenfrost point of the new case resulted to be lower than the one of 9 μl size, as shown in Figure 5.3.
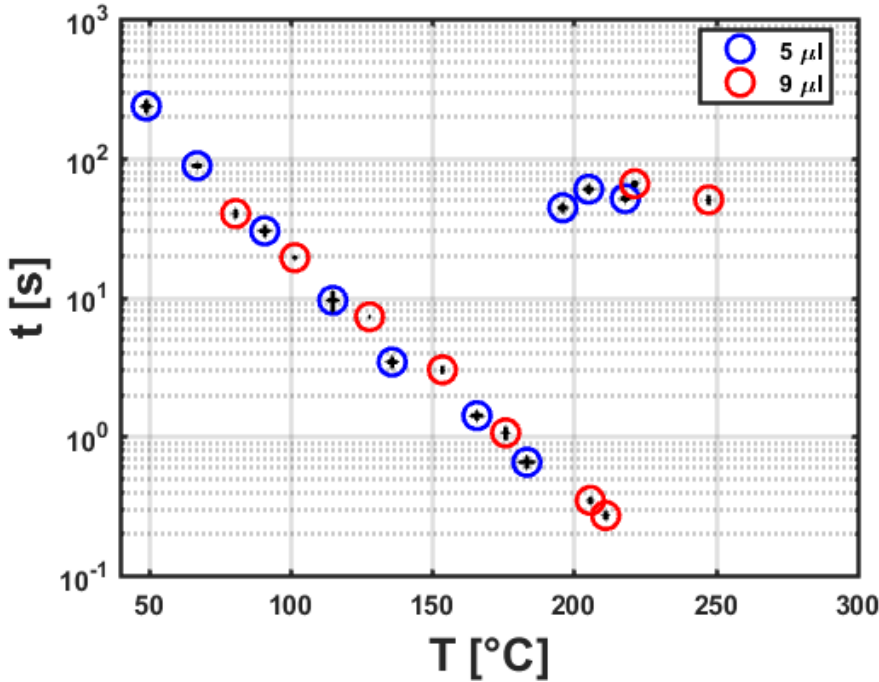

Figure 5.3: Validation of the evaporation design

Since the LFP is proportional to the droplet size, the result is then consistent with the previous study[48, 11].

5.4   Experimental uncertainty

The uncertainties are mostly related to the temperature. The error analysis was the same applied from the previous work[11], with an improvement

done for the systematic uncertainty coming from the calibration. As well as done in the section 3.2.6, the non linearity, accuracy and repeteability errors were computed. Also here, Figure 5.4 was useful to compute the non linearity and accuracy uncertainties. The graph are just referred to one of the thermocouples.
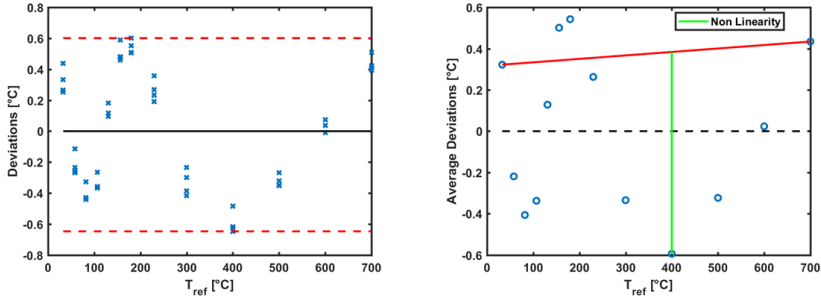
Figure 5.4: (a) Accuracy (b) Non linearity

By applying the equation 3.5, the systematic errors were computed and summarized in Table 5.1.

Table 5.1: Calibration uncertanties of the different thermocouples

	T_1	T_2	T_3
B_T [°C]	1.77	1.70	1.77

5.5   Results and discussion

The experiment was performed up to the start of the transition boiling region, as reported in Figure 5.5. Droplet lifetime versus surface temperature were measured. In order to make a good comparison the same temperatures were considered.

Figure 5.5: Evaporation curve with reference to the Plain Si

All the nanowires show an enhancement of the droplet cooling performance, which comes from a reduction in the droplet evaporation time. This can be explained by looking at the dynamics of the droplet. Figure 5.6 shows what occurs in the range of temperatures below the T_{sat}. For completeness, the dynamics is shown from both the front and the top camera.
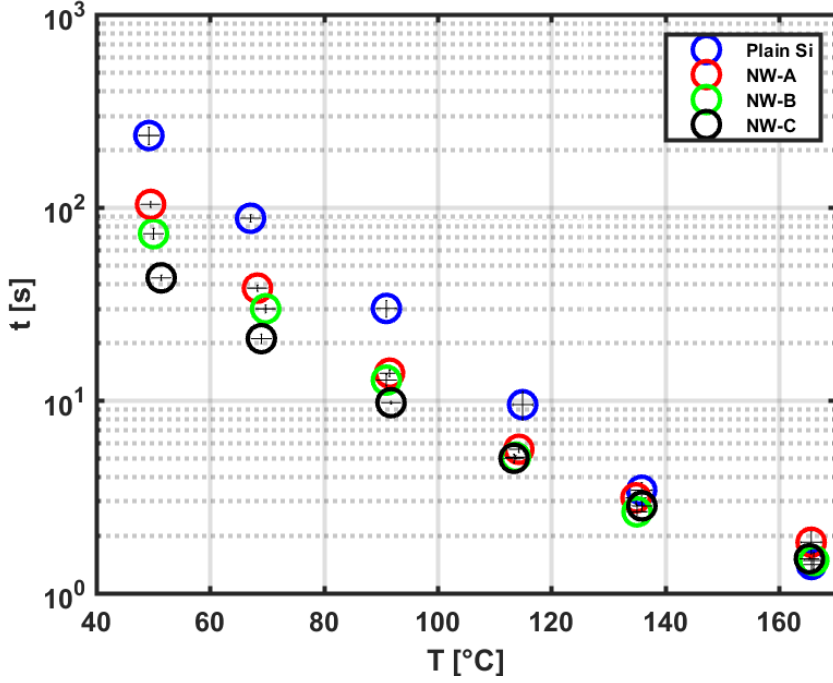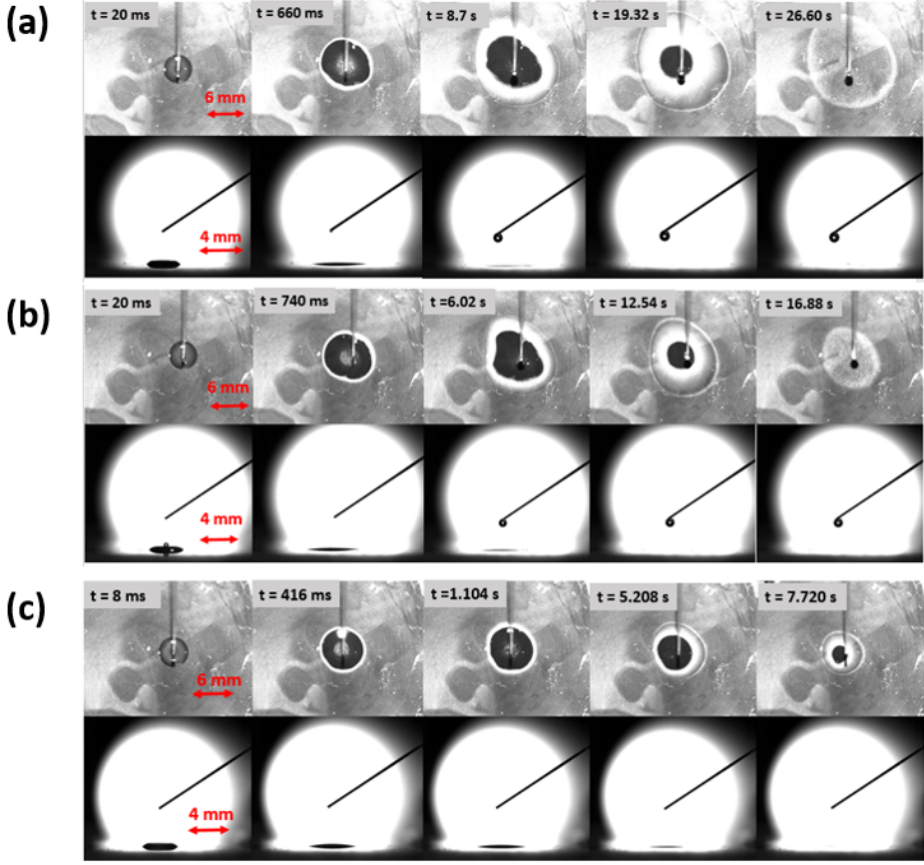
Figure 5.6: Dynamics of the droplet in the evaporation regime for NW-C (a)T = 51 °C (b)T = 69 °C (c)T = 92 °C

For all the three cases, the droplet starts spreading and the formation of the precursor rim occurs. However, the bulk drainage is occuring only for the two first temperatures. The increase of the temperature results in a lower spreading area of the precursor rim. Furthermore, it is interesting to observe that the precursor rim and an upper droplet with low contact angle are noticeable only from the top view camera. That is important for an accurate measurement of the droplet lifetime. For example, Figure 5.6 (a) shows that the top camera still shows the precursor rim in the last two frames, after more than 10 seconds from the third frame. From a thermodynamics point of view, the better heat transfer performance might be due to the increase of the exchange area(increase of roughness) and to the reduction of

thermal resistance (lower thickness of the precursor rim). Above saturated conditions, the cavity present on the nanowires surface start to be activated and release bubbles. This phenomenon is known as nucleate boiling, and becomes more intensive as the surface temperature increases(as shown in Figure 5.7).
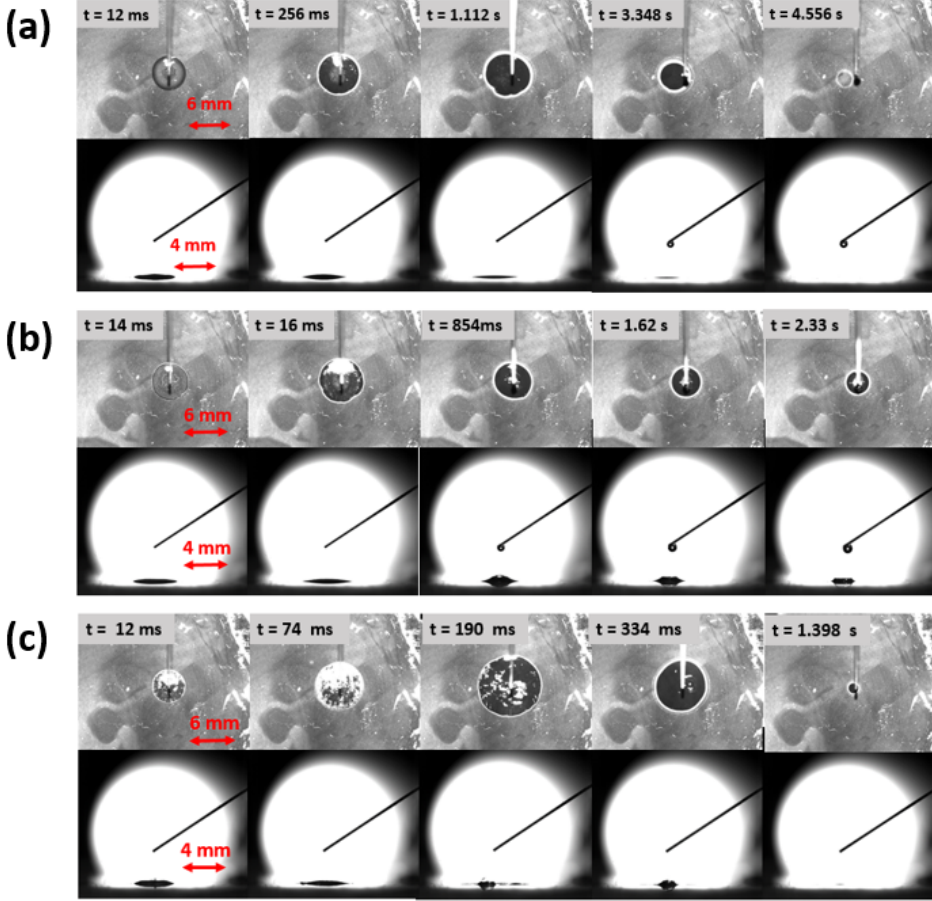
Figure 5.7: Dynamics of the droplet in the nucleate boiling regime for NW-C (a)T = 113 °C (b)T = 136 °C (c)T = 165 °C

Despite the increase of temperature, the precursor rim is still present due to the wicking of the sample. In the case of the plain silicon surface, evaporation is occuring below the saturation temperature and no precursor rim has formed due to the absence of wicking, as shown in Figure 5.8.
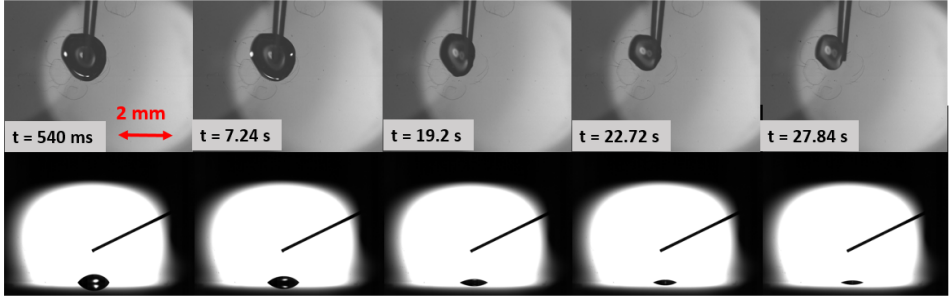
Figure 5.8: Dynamics of the droplet in the evaporation regime for Plain Si at T = 92 °C

This results in a lower spreading area that explains the higher evaporation time. Nucleate boiling is occuring above the saturation temperature, as shown in Figure 5.9.
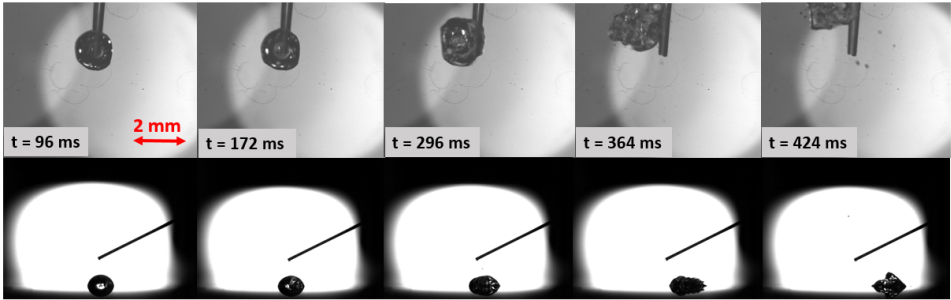
Figure 5.9: Dynamics of the droplet in the nucleate boiling regime for Plain Si at T = 136 °C

By looking at Figure 5.5 it can be observed that the increase of surface temperature results in the intersection of the evaporation curves. Figure 5.10 compares the nanowires performance with respect to the plain silicon versus the surface temperature. With regard to the evaporation regime, the nanowires with highest wicking show a best reduction in the evaporation time of about 82 %, 76 % and 68 % at respectively 51, 69 and 92 °C. In the nucleate boiling regime, Si nanowires still show a better cooling performance even though the wicking plays a less dominant role, due to the onset of the phase change. In particular, at a temperature of 165 °C the plain silicon shows a lower cooling time.
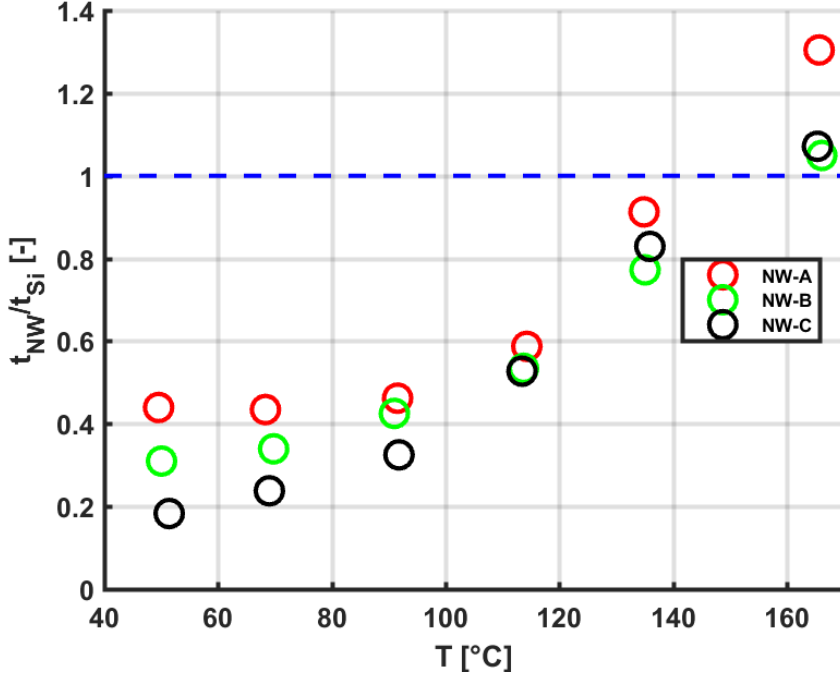
Figure 5.10: Cooling time of NWs (normalized to the cooling of plain Si) versus surface temperature

This could be explained by considering the balance between the wicking and evaporation/boiling forces. As the temperature increases, the wicking force is suppressed due to the decrease of the surface tension with the temperature [49], while the boiling force gets more dominant. In regard of this result, the nanowicking results to be fundamental in enhancing the cooling of the evaporation regime and nucleate boiling (up to some critical temperature). Although plain silicon has a better performance for higher temperature, the margin from the safety limit is narrow. In fact, nanowires extend the transition boiling region, as shown in previous work [11], they represent a more efficient and safer solution for the thermal management applications.

Finally, random Si nanowires have shown a lower evaporation time with respect to what can be found in the literature. Hsieh et al. performed an experiment of a single droplet DI water impinged on a patterned Si micropillar sample[42]. They have found a decrease of 45 % at 80 °C of the droplet lifetime with respect to the plain Si, our sample showed a decrease of

68 % even at higher temperatures. Further, by considering the fabrication process, random Si NWs represent a better choice. Infact, the process is very simple and cheap.

Chapter 6

Conclusions and further work

In this thesis, the effect of the wicking on the evaporation curve has been assessed. In the evaporation regime, the nanowires with highest wicking (w = 0.888 ± 0.076 mm/s$^{0.5}$) showed an significant decrease in the cooling time with respect to the Plain Si of 82 %, 76 % and 68 % at 51 °C, 69 °C and 92 °C. It can be concluded that the higher is the wicking, the lower is the cooling time in the evaporation/nucleate regime. Moreover, this is true up to a critical temperature where the wicking forces are less dominant. Further, Si random NWs have shown the lowest cooling time with respect to the literature[42], in which the reduction of the Si patterned microstructures was 45 % with respect to the plain Si.

Since the spreading area and the contact angle are important for characterizing the surface prior the heat transfer experiment, synchronous measurements of three random Si nanowires with three different heights were performed. It has been assessed that the tallest nanowires show the best wicking performance.

A general method to characterize the wettability and wickability for super-hydrophilic surfaces has been provided. The method was validated by using a standard paper with a known flow rate. The flow rate given by our method differentiates for a maximum of 9 %. Further, it has been shown that the area approach is strongly recommended with respect to the point approach. According to the previous work [32], it has been observed that wicking source could play an important role for this phenomenon.

As recommendation for further work, the effect of the wicking on the Leidenfrost point could be investigated. It would be interesting also to assess the effect of temperature on wettability and wickability in the evaporation region. Finally, as part of this project, the wickability and evaporation performance of Si patterned nanowires would be assessed.

Bibliography

[1] Ho Seon Ahn, Gunyeop Park, Joonwon Kim, and Moo Hwan Kim. Wicking and Spreading of Water Droplets on Nanotubes. *Langmuir*, 28(5):2614–2619, 2012.

[2] Xue Chen, Jiannan Chen, Xiaolong Ouyang, Yu Song, Ruina Xu, and Peixue Jiang. Water Droplet Spreading and Wicking on Nanostructured Surfaces. *Langmuir*, 33(27):6701–6707, 2017.

[3] John R. Thome. The New Frontier in Heat Transfer: Microscale and Nanoscale Technologies. *Heat Transfer Engineering*, 27(9):1–3, oct 2006.

[4] Bruno Agostini, Matteo Fabbri, Jung E. Park, Leszek Wojtan, John R. Thome, and Bruno Michel. State of the Art of High Heat Flux Cooling Technologies. *Heat Transfer Engineering*, 28(4):258–281, apr 2007.

[5] Neelesh A. Patankar. Supernucleating surfaces for nucleate boiling and dropwise condensation heat transfer. *Soft Matter*, 6(8):1613, 2010.

[6] Zhonghua Yao, Yen-Wen Lu, and Satish G. Kandlikar. Direct growth of copper nanowires on a substrate for boiling applications. *Micro & Nano Letters*, 6(7):563, 2011.

[7] Renkun Chen, Ming-Chang Lu, Vinod Srinivasan, Zhijie Wang, Hyung Hee Cho, and Arun Majumdar. Nanowires for enhanced boiling heat transfer. *Nano letters*, 9(2):548–53, feb 2009.

[8] Jorge Padilla and Van P Carey. WATER DROPLET VAPORIZATION ON SUPERHYDROPHILIC NANOSTRUCTURED SURFACES AT HIGH AND LOW SUPERHEAT. In *Proceedings of the ASME 2014 International Mechanical Engineering Congress and Exposition*, pages 1–15, 2014.

[9] Claire M Kunkle, Jordan P Mizerak, and Van P Carey. Ht2017-4847 the Effects of Wettability and Surface Morphology on Heat. pages 1–10, 2017.

[10] Wei Tong, Lu Qiu, Jian Jin, Lidong Sun, and Fei Duan. Unique lift-off of droplet impact on high temperature nanotube surfaces. *Applied Physics Letters*, 111(9), 2017.

[11] Manuel Auliano, Maria Fernandino, Peng Zhang, and Carlos Alberto Dorao. Water droplet impacting on overheated random Si nanowires. *International Journal of Heat and Mass Transfer*, 124:307–318, 2018.

[12] Dong Hwan Shin, Seong Hyuk Lee, Chang Kyoung Choi, and Scott Retterer. The evaporation and wetting dynamics of sessile water droplets on submicron-scale patterned silicon hydrophobic surfaces. *Journal of Micromechanics and Microengineering*, 20(5), 2010.

[13] L. H.J. Wachters and N. A.J. Westerling. The heat transfer from a hot wall to impinging water drops in the spheroidal state. *Chemical Engineering Science*, 21(11):1047–1056, 1966.

[14] Gangtao Liang and Issam Mudawar. Review of drop impact on heated walls. *International Journal of Heat and Mass Transfer*, 106(March):103–126, 2017.

[15] J. D. Bernardin and I. Mudawar. The Leidenfrost Point: Experimental Study and Assessment of Existing Models. In *Journal of Heat Transfer*, volume 121, page 894, 1999.

[16] Manuel Auliano, Maria Fernandino, Peng Zhang, and Carlos Alberto Dorao. The Leidenfrost phenomenon on sub-micron tapered pillars. In *ASME. International Conference on Nanochannels, Microchannels, and Minichannels, ASME 2017 15th International Conference on Nanochannels, Microchannels, and Minichannels*, pages 1–9, 2017.

[17] Van P. Carey. Liquid-Vapor Phase-Change Phenomena. In Summers Scholl, editor, *Liquid-Vapor Phase-Change Phenomena*, chapter 8, pages 359–371. Second edition, 2008.

[18] Abraham Marmur, Claudio Della Volpe, Stefano Siboni, Alidad Amirfazli, and Jaroslaw W. Drelich. Contact angles and wettability: towards common and accurate terminology. *Surface Innovations*, 5(1):3–8, 2017.

[19] Claire K. Wemp and Van P. Carey. Water Wicking and Droplet Spreading on Randomly Structured Thin Nanoporous Layers. *Langmuir*, 33(50):14513–14525, 2017.

[20] Seol Ha Kim, Ho Seon Ahn, Joonwon Kim, Moo Hwan Kim, and Hyun Sun Park. Experimental study of water droplets on over-heated nano/microstructured zirconium surfaces. *Nuclear Engineering and Design*, 278:367–376, oct 2014.

[21] Xianliang Sheng and Jihua Zhang. Superhydrophobic behaviors of polymeric surfaces with aligned nanofibers. *Langmuir*, 25(12):6916–6922, 2009.

[22] C. Ding, P. Bogorzi, M. Sigurdson, C.D. Meinhart, and N.C. MacDonald. Wicking optimization for thermal cooling -with a titanium based heat pipe system. In *Hiltonhead Conference 2010, Solid-State Sens., Actuators, Microsyst. Workshop*, page 376, 2010.

[23] Christopher Oshman, Qian Li, Li-anne Liew, Ronggui Yang, Y C Lee, Victor M Bright, Darin J Sharar, Nicholas R Jankowski, and Brian C Morgan. Thermal performance of a flat polymer heat pipe heat spreader under high acceleration. *Journal of Micromechanics and Microengineering*, 22(045018):12, 2012.

[24] Changchun Liu, Michael G Mauk, Robert Hart, Xianbo Qiu, and Haim H Bau. A self-heating cartridge for molecular diagnostics. *Lab on a Chip*, 11:2686–2692, 2011.

[25] Nathan Lazarus, Sarah S Bedair, Chiung-c Lo, and Gary K Fedder. CMOS-MEMS Capacitive Humidity Sensor. *Journal of Microelectromechanical Systems*, 19(1):183–191, 2010.

[26] S. Chandra and C. T. Avedisian. Observations of droplet impingement on a ceramic porous surface. *International Journal of Heat and Mass Transfer*, 35(10):2377–2388, 1992.

[27] Md Mahamudur Rahman, Emre ??l??eroglu, and Matthew McCarthy. Role of wickability on the critical heat flux of structured superhydrophilic surfaces. *Langmuir*, 30(37):11225–11234, 2014.

[28] Dong Il Shim, Geehong Choi, Namkyu Lee, Taehwan Kim, Beom Seok Kim, and Hyung Hee Cho. Enhancement of Pool Boiling Heat Transfer using Aligned Silicon Nanowires Array. 2017.

[29] Beom Seok Kim, Geehong Choi, Dong Il Shim, Kyung Min Kim, and Hyung Hee Cho. Surface roughening for hemi-wicking and its impact on convective boiling heat transfer. *International Journal of Heat and Mass Transfer*, 102:1100–1107, 2016.

[30] Taylor P Allred, Justin A Weibel, and Suresh V Garimella. A Wettability Metric for Characterization of Capillary Flow on Textured Superhydrophilic Surfaces. *Langmuir*, 33(32):7847–7853, 2017.

[31] M. Parada, D. Derome, R. M. Rossi, and J. Carmeliet. A review on advanced imaging technologies for the quantification of wicking in textiles. *Textile Research Journal*, 87(1):110–132, 2017.

[32] P.R. Harnett and P.N. Mehta. A Survey and Comparison of Laboratory Test Methods for Measuring Wicking. *Textile Research Journal*, 54(7):471–478, 1984.

[33] Beom Seok Kim, Hwanseong Lee, Sangwoo Shin, and Hyung Hee Cho. Interfacial wicking dynamics and its impact on critical heat flux of boiling heat transfer. *Applied Physics Letters*, 105(191601), 2014.

[34] J Fan and Y Zhao. Spreading of a water droplet on a vertically aligned Si nanorod array surface. *Applied Physics Letters*, 013102(2007), 2007.

[35] Edward W. Washburn. THE DYNAMICS OF CAPILLARY FLOW. *Phisical Review*, XVII(3), 1921.

[36] Trong Thi Mai, Chang Quan Lai, H. Zheng, Karthik Balasubramanian, K. C. Leong, P. S. Lee, Chengkuo Lee, and W. K. Choi. Dynamics of wicking in silicon nanopillars fabricated with interference lithography and metal-assisted chemical etching. *Langmuir*, 28(31):11465–11471, 2012.

[37] Conan Zhang and Carlos H Hidrovo. Investigation of nanopillar wicking capabilities for heat pipes applications. In *ASME 2009 Second Int. Conf. Micro/Nanoscale Heat Mass Transfer*, pages 423–437, 2009.

[38] Md Mahamudur Rahman, Emre Ölçeroglu, and Matthew McCarthy. Role of wickability on the critical heat flux of structured superhydrophilic surfaces. *Langmuir*, 30(37):11225–11234, 2014.

[39] Seong Jin Kim, Myoung Woon Moon, Kwang Ryeol Lee, Dae Young Lee, Young Soo Chang, and Ho Young Kim. Liquid spreading on superhydrophilic micropillar arrays. *Journal of Fluid Mechanics*, 680:477–487, 2011.

[40] Zhonghua Yao, Yen-Wen Lu, and Satish G. Kandlikar. Direct growth of copper nanowires on a substrate for boiling applications. *Micro & Nano Letters*, 6(7):563, 2011.

[41] Fanghao Yang, Xianming Dai, Yoav Peles, Ping Cheng, and Chen Li. Can multiple flow boiling regimes be reduced into a single one in microchannels? *Applied Physics Letters*, 103(4), 2013.

[42] Cheng Chieh Hsieh and Shi Chune Yao. Evaporative heat transfer characteristics of a water spray on micro-structured silicon surfaces. *International Journal of Heat and Mass Transfer*, 49(5-6):962–974, 2006.

[43] Bo Shi, Yi-Biao Wang, and Kai Chen. Pool boiling heat transfer enhancement with copper nanowire arrays. *Applied Thermal Engineering*, 75:115–121, jan 2015.

[44] Dong Hwan Shin, Seong Hyuk Lee, Jung Yeul Jung, and Jung Yul Yoo. Evaporating characteristics of sessile droplet on hydrophobic and hydrophilic surfaces. *Microelectronic Engineering*, 86(4-6):1350–1353, 2009.

[45] Mathworks. Matlab website.

[46] Anthony J. Wheeler and Ahmad R. Ganji. Experimental Uncertainty Analysis. In *Introduction to Engineering Experimentation*, pages 209–253. Pearson, third edition.

[47] Manuel Auliano, Maria Fernandino, Peng Zhang, and Carlos Alberto Dorao. ICNMM2016-8032. In *ASME. International Conference on Nanochannels, Microchannels, and Minichannels, ASME 2016 14th International Conference on Nanochannels, Microchannels, and Minichannels*, pages 1–8, 2016.

[48] Anton Hassebrook, Corey Kruse, Chris Wilson, Troy Anderson, Craig Zuhlke, Dennis Alexander, George Gogos, and Sidy Ndao. Effects of droplet diameter on the Leidenfrost temperature of laser processed multiscale structured surfaces. *Fourteenth Intersociety Conference on Thermal and Thermomechanical Phenomena in Electronic Systems (ITherm)*, pages 452–457, may 2014.

[49] Conan Zhang and CH Hidrovo. Nanoscale Wicking Structures. *Asme 2009 . . .* , pages 1–14, 2009.